Fall 2014

Characterization of 304L stainless steel by means of minimum input energy on the selective laser melting platform

Ben Brown

Department:

CHARACTERIZATION OF 304L STAINLESS STEEL BY MEANS OF MINIMUM INPUT ENERGY ON THE SELECTIVE LASER MELTING PLATFORM

By

BEN BROWN

A THESIS

Presented to the Faculty of the Graduate School of the

MISSOURI UNIVERSITY OF SCIENCE AND TECHNOLOGY

In Partial Fulfillment of the Requirements for the Degree

MASTER OF SCIENCE MANUFACTURING ENGINEERING

2014

Approved by

Frank Liou, Advisor
Joseph Newkirk
Edward Kinzel

All data prepared, analyzed and presented has been developed in a specific context of work and was prepared for internal evaluation and use pursuant to that work authorized under the referenced contract. Reference herein to any specific commercial product, process or service by trade name, trademark, manufacturer, or otherwise, does not necessarily constitute or imply its endorsement, recommendation, or favoring by the United States Government, any agency thereof or Honeywell Federal Manufacturing & Technologies, LLC.

This presentation has been authored by Honeywell Federal Manufacturing & Technologies under Contract No.DE-NA0000622 with the U.S. Department of Energy. The United States Government retains and the publisher, by accepting the article for publication, acknowledges that the United States Government retains a nonexclusive, paid up, irrevocable, world-wide license to publish or reproduce the published form of this manuscript, or allow others to do so, for the United States Government purposes

ABSTRACT

Developing parameter sets for new materials on the Selective Laser Melting (SLM) platform has traditionally been done through the use of single line processing windows and a basic design of experiments (DOE) which would include varying machine parameters to maximize density. This study expands the traditional method by determining the main effects statistically for density, allowing for a more in depth analysis wherein the experimental results are statistically correlated to the variable machine parameters used. With this analysis, parameter optimization with respect to achieving near full density, while also considering build rates, can be performed. New parameters for 304L stainless steel were developed using this method on a Renishaw AM250. Single line processing windows were used to determine bounds on machine parameters. Utilizing this information, a DOE was implemented in which density samples were fabricated and the statistical main effects on density were derived. Several methods for density determination were also investigated as part of this study. In order to quantify machine parameters, a novel energy density term was formulated. Optimal parameter sets were found and energy density was reduced to increase build rate. Sensitivity of mechanical properties to the reduction was shown to be minimal over the range tested. Finally, the effect of decreased energy density on microstructure, part density, mechanical properties, and orientation sensitivity were then measured.

ACKNOWLEDGEMENTS

I would like to extend thanks to my advisor, Dr. Frank Liou, who helped to guild me in my project. I would also like to thank Dr. Joseph Newkirk and Dr. Edward Kinzel for serving on my committee. Thanks to my numerous coworkers at Honeywell for their assistance in my project. Finally, thanks to my family and friends for their support.

TABLE OF CONTENTS

Page

LIST OF ILLUSTRATIONS

Page

LIST OF TABLES

Page

NOMENCLATURE

Symbol	Description
P	Laser Power
v	Scan Velocity
s	Spot Diameter
ss	Spot Size
d	Spot Overlap
h	Layer Thickness
hs	Hatch Spacing
pd	Point Distance
et	Exposure Time
HR	Hausner Ratio
ρ_T	Tapped Density
ρ_B	Bulk Density
P_ρ	Power Density
$E_{\rho 1}$	Single Point Energy Density
$E_{\rho 2}$	Two Dimensional Energy Density

1 INTRODUCTION AND LITERATURE REVIEW

1.1 INTRODUCTION TO SLM

Selective Laser Melting (SLM) also known as Direct Metal Laser Sintering (DMLS) or LaserCUSING is an Additive Manufacturing (AM) process that uses a laser in an inert atmosphere to selectively melt layers of loose metal powder into a solid, building a part layer by layer from the bottom up. AM is a recent innovation in manufacturing technology with development beginning in the mid 1980's[1]. The first AM methods developed were the polymer technologies such as Stereolithography in 1984 and Selective Laser Sintering (SLS) in 1986. The same principles that made these polymer technologies possible were eventually applied to metal materials and technologies such as Directed Energy Deposition, Electron Beam Melting (EBM), and SLM were later developed. Parts processed on AM machines use a 3D CAD file that has been sliced into layers that the machine reads and either scans or deposits material on the identified interior of the part. This process is repeated for each layer until the build is complete.

Regardless of material, all AM technologies give designers a unique ability to build parts that were previously considered uneconomical to produce or even unmanufacturable. In the medical industry, the ability to build organic shapes and economically produce bespoke components that fit the patient opens many new possibilities for more functional orthopedic and dental implants [1-6]. In the general manufacturing industry, AM gives an opportunity for innovative ways to reduce weight and design parts that are not limited to traditional manufacturing limitations [1, 5-8]. In

order to fully realize these benefits, the current pallet of available and characterized materials needs to be expanded. In doing so, the usage of AM processes can be expanded.

The Renishaw AM250 Laser Melting Machine is a commercially available SLM machine that was used in this research. A diagram of its build chamber can be seen in Figure 1.1.

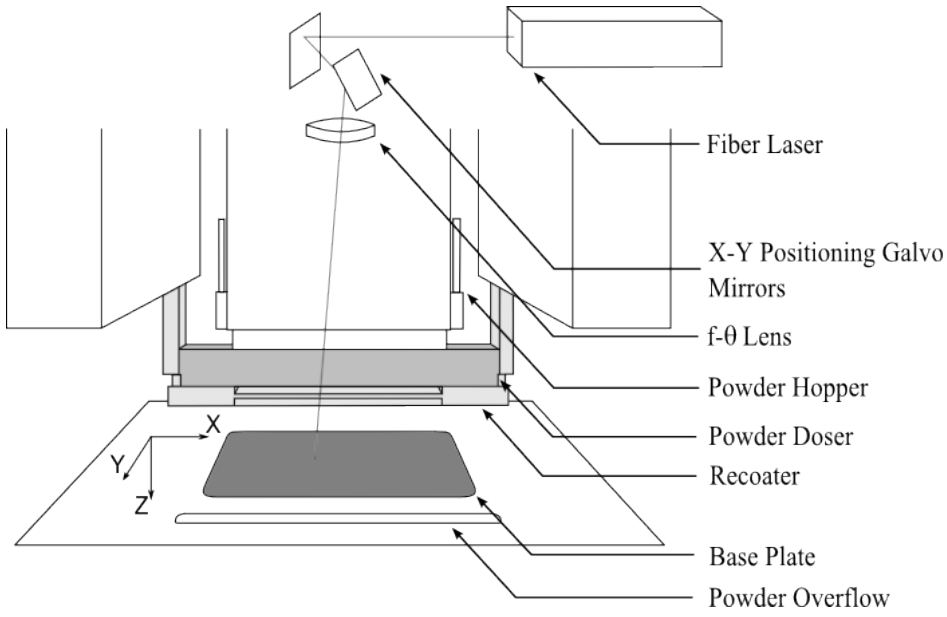

Figure 1.1: Renishaw AM250 SLM Machine Chamber Diagram

On this machine, the process of building a part begins with a base plate being bolted to an elevator that moves along the Z axis. A recoater depresses springs on a powder doser, allowing powder to be deposited from the hopper in front of the recoater. The elevator is dropped a layer thickness and the recoater is brought forward, laying

down a single layer of powder with any excess powder being deposited in the powder overflow. A laser beam is then positioned by mirrors through an f-θ lens where it is focused at the powder bed and the material is melted into the part layer. The laser scans each part layer in a predetermined pattern, illustrated in Figures 1.2 and 1.3.

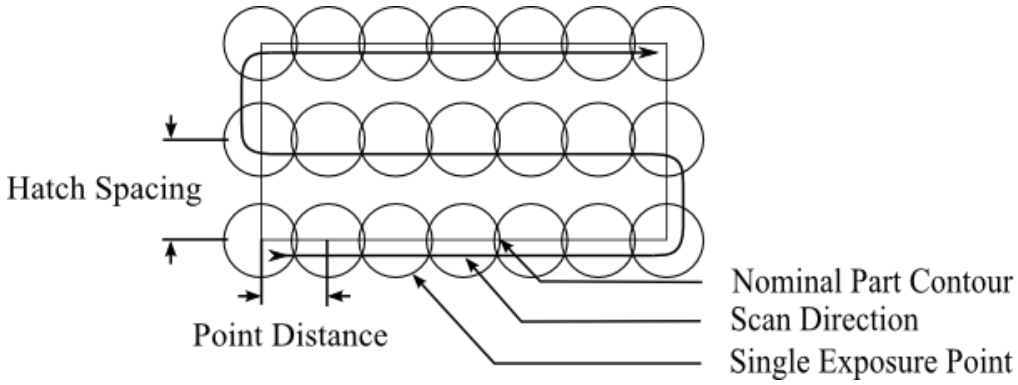

Figure 1.2: Spot Exposure Scan Pattern

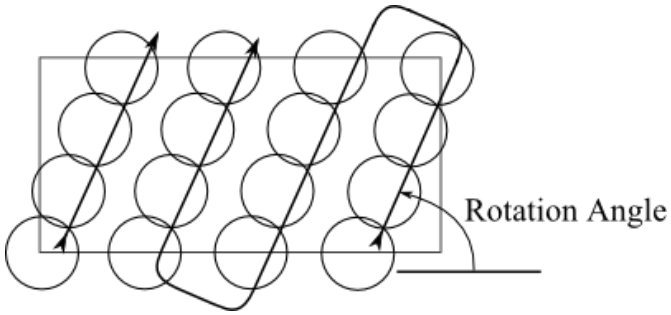

Figure 1.3: Scan Pattern After Layer Rotation

The Renishaw AM250 uses a point exposure scan pattern where a single point is exposed, the laser is turned off, repositioned, and then the next point is exposed. The spot exposure strategy allows the AM250 to build finer detail features as a static melt pool is more stable than a dynamic one. A meandering pattern as seen in Figure 1.2 is used to scan each layer. After the layer is completed, the recoater is the returned to the powder doser and the process repeats. When the next layer is scanned, the same pattern as used in the previous layer is rotated and translated a specified amount to prevent the same points from being exposed multiple times in subsequent layers. An example of this modified pattern can be seen in Figure 1.3.

The scan pattern illustrated is the simplest example of the patterns that are used. Here, there is no compensation used for the diameter of the beam and the scan is a simple meander pattern. There are no finishing passes along the contour of each layer to create a watertight part with a better surface finish. This simple pattern is representative of what is used for bulk fill of components. Other common scan strategies implement segmenting the build area into stripes or a chessboard-like pattern and meandering the laser path within these segments. Other machine manufactures such as EOS GmbH, SLM Solutions GmbH, or Concept Laser GmbH use a similar build chamber setup. Machines produced by 3D Systems differ slightly in machine setup, as material is rolled and compacted as opposed to being spread over the build plate. For all of these machines, the laser is continuously on when exposing a layer. Currently the Renishaw system is the only commercial machine to use the point exposure scan strategy. Of the commercially available systems, most have a similar build volume and laser source. A sample of machine offerings can be seen below in Table 1.1.

Table 1.1: Selected Machine Build Volume and Laser Type [9]

Manufacturer (Model)	Build Volume (mm)	Laser Power (Watts)
EOS (M280)	250 x 250 x 325	200 or 400
Concept Laser (M2)	300 x 350 x 300	200 or 400
3D Systems (PXL)	250 x 250 x 300	500
Renishaw (AM 250)	245 x 245 x 360	200
SLM Solutions (SLM 280)	280 x 280 x 350	Dual 400/1000

1.2 CURRENT METHOD OF MATERIAL DEVELOPMENT

For the SLM platform, the current method for the development of new materials is done utilizing a Design of Experiments (DOE) varying machine parameters with the goal of producing a near fully dense part. This can initially be carried out in the form of determining a processing window, varying laser power and scan speed for single line scans. From this 1D analysis to the development of 3D parts, the additional primary parameters that have been varied are scan spacing, and layer thickness [10-28]. Secondary parameters such as shield gas composition, laser spot size, preheat temperature, etc. are generally not varied and are determined by setup limitations. In the building of 3D parts, scan pattern has also been shown to have an effect on the mechanical properties and surface finish, and been analyzed for many materials [12, 14, 16-18, 21, 26, 29, 30]. In addition to manipulating machine parameters to achieve full density, the usage of layer remelting has been shown to refine the grain structure and

improve density [31-33]. The process of Hot Isostatic Pressing (HIP) completed parts has also been shown to improve part density [34].

Numerous pure metals and alloys have been characterized on the SLM platform including iron [13-15, 27, 30, 35], copper [20, 36], stainless steels [15, 20, 21, 25, 31, 37-42], aluminum [28, 33], tool steels [15, 20, 40, 41], tungsten [19], Co-Cr [3, 4, 20, 22, 23], nickel based super alloys such as Waspaloy® [17] and Inconel [20], magnesium [11, 43], and titanium [12, 24, 44]. Of all the materials that have been developed, the material of interest, 304L stainless steel, has not been found in any literature.

The DOE method is effective for finding a parameter sets that work for the given material and mapping the regions where these parameters are effective. However, there is not a well-defined and developed process for determining an optimal set of machine parameters within the determined processing window or mapping the resulting mechanical properties across processing window regions. In addition, this basic method does not give insight for the optimization of parameter sets.

1.2.1 Processing Windows. As previously mentioned, results of the DOE varying the laser power levels and laser scan speed, a processing window can be constructed and has been used for the development of many materials [11, 17-19, 23, 27, 28, 30, 40, 43]. This is a common practice that allows for easy determination of processing regions. These different regions show where parameters have the same general effect on the material and can be characterized as either showing vaporized material, fully melted material, or not fully melted material. In the case of vaporized material, the laser power is too high for the given scan speed. This leads to melt pools that show a distinct discoloration and the possibility having the presence of keyhole mode

welding in the bed. It has been shown that keyhole mode melting can lead to added porosity [45]. On the other end of the failure mode spectrum, material can be not fully melted. This is where at the given laser power the scan speed is too high. Here, the melt pools could make an incomplete track where the material has balled. The mechanism of balling has been well explored [18, 36] and the cause can be described as high surface tension causing the material to form the lowest energy geometry and "ball" into spheres. In addition, this region might also show where scan tracks do not fully adhere to the base plate. In between these two regions, there is a region of what can be assumed to be good processing parameters where solid scan tracts are formed and conduction mode heat transfer has bonded the scan tract to the substraight.

1.2.2 Input Quantification Terms. In order to quantify the multiple machine parameters being varied into a single parameter, a term most commonly known as energy density is often formulated. There are many formulation methods that have been presented when developing material on the SLM platform. These terms range from one to three dimensions and include many of the primary variables discussed in the previous sections.

A simple linear energy density [18, 21] or input energy per unit speed [16] has been used to quantify laser power and laser scan speed. This 1D formulation can be seen as Equation 1 where P is laser power is and v is laser scan speed.

$$\lambda = \frac{P}{v} \quad (1)$$

A similar formulation was used by Ng [43]. The addition of the size of the laser spot diameter creates a 2D term as in Equation 2 where P is laser power is, v is laser scan speed, and s is laser spot diameter.

$$E_\rho = \frac{P}{s \cdot v} \quad (2)$$

Simchi [14, 15] gives a 3D specific energy input in $\frac{\mathrm{J}}{\mathrm{mm}^3}$ by combining laser power, laser scan speed, powder layer thickness h , and scan overlap d as seen in Equation 3. This formulation is the most commonly used in literature.

$$\psi = \frac{P}{v \cdot h \cdot d} \quad (3)$$

Olakanmi [28] also uses this formulation. Gu [19] and Thijis [26] refer to this as volumetric energy density ε and Kruth [13] refers to this as Laser Density (LD). Simchi also use a specific energy input that reflects the energy per volume of laser track $\overline{\mathrm{Q}}$ in $\frac{\mathrm{J}}{\mathrm{mm}^3}$ [15]. This is done by compensating for the overlap within a specific volume. Coupling efficiently η is also introduced and the final formulation can be seen in Equation 4.

$$\overline{Q} = \frac{\pi \cdot \eta \cdot P}{4 \cdot h \cdot v \cdot d} \quad (4)$$

This formulation is unique as it uses a term to attempt to quantify losses in the system.

All of the presented formulations quantify input parameters for a continuous wave laser, being treated as remaining continuously on when exposing a layer. For this

research where a point exposure scan strategy is being used, a different approach needs to be used to quantify machine parameters. These operating parameters lead to a static melt pool as opposed to a dynamic one, similar to what is used in laser spot welding. With this connection many similarities can be drawn for quantification formulations.

Laser spot welding is generally characterized for a single exposure point by the machine parameters laser power and laser spot size. These terms are quantified into term known as power density [46-48] as formulated in Equation 5 where P is laser power is and s is laser spot size.

$$P_\rho = \frac{P}{ss} \quad (5)$$

1.2.3 Varying Effects of Energy Input. As energy input increases, there are three identified modes of laser welding; conductive, transitional, and keyhole [47]. In a continuous wave laser weld, there are clear transitions between the three modes. With a laser pulse on the order of milliseconds, penetration depth is linearly proportional to laser power and there is no clear separation between the three modes [47]. This effect seen in laser welding has also been demonstrated in SLM [45].

It has been shown in numerous studies that there is a direct correlation between input energy and the resulting density of the part where as input energy increases, so does part density. There is a point where increased input energy no longer increases part density [28, 35, 37, 49] or in other cases actually decreases resulting density [11, 19, 21]. Kempen et al. [33] shows in AlSi10Mg if the relationship of energy input and relative density is clarified, that density does in fact begin to drop. In both cases, there is a “cusp” where additional energy no longer increases the density of the part being built.

It has also been shown that with increased input energy, the average grain size also increases [50] decreasing mechanical properties. Not only does the size of the grain change, but the shape of the grain is also a function of machine parameters. Niendoef et al. [51] shown that at higher laser power inputs grains become more columnar and at low powers become more equiaxed. Another study showed that when the same region is exposed multiple times causing a region to retain heat, columnar grains form [52].

Determining the required energy to reach the cusp can be difficult to model because not all of the input energy is absorbed into the system and that there is in fact an input to melt ratio in AM processes [53].

1.3 POWDER REQUIRMENTS

In the solidification of a porous powder bed, the bed is melted and condenses into a near fully dense layer when enough energy is added [38]. In order to achieve a fully dense melted layer, a high initial layer density is required. Size distribution and morphology of the powder determine the packing efficiency of the powder bed.

With spherical particles of uniform size, full density is not achievable due to voids between particles. In addition, there are also losses in achievable density created due to the wall effect where voids are created by spherical particles contact a flat surface [54]. However, because surface roughness is effected by particle size [55], this effect decreases when powder is deposited on a previously built layer [56]. In order to mitigate these effects, a distribution of particle size is needed where small particles fill in the voids created by larger particles contacting one another. With different distributions of size, certain phenomena are noticed. With a narrow particle size range the powder tends to agglomerate, leading to difficulty is powder deposition. With a large range the powder

tends to segregate leading to non-uniform deposition [35]. It has been shown that powder bed composition has an effect on the required input energy to melt the powder bed [35, 38].

For powder to pack well in a powder bed, it needs to flow well. The ratio of tap density to bulk density, known as the Hausner Ratio, is an effective approximation of friction between particles and therefore of flowability of powder [57]. Tap density is defined as the measured bulk density after a "tapping" of the material, allowing for powder to settle and compact. As the Hausner Ratio increases, flowability decreases. Hausner ratio is dependent on size distribution and shape of the particles. The formulation for Hausner ratio can be seen below in Equation 6.

$$HR = \frac{\rho_T}{\rho_B} \quad (6)$$

In addition to the physical characteristics of the powder to achieve dense parts, chemical composition also affects the final product. Powder beds with a high oxygen content in either the powder or build atmosphere deteriorate build quality and density [58]. Variance in the chemical composition of the powder has also been shown to effect the final phase of the part due to phase stabilizers and cooling rates [59].

2 PREVIEW OF EXPERIMENTS

The purpose of these experiments is to prove that an ideal parameter set can be determined more specifically through the DOE method by identifying minimum energy input to still achieves acceptable mechanical properties. To investigate this, the full processing window will be developed with single line scans. A three level DOE investigating the four major machine parameters will then be conducted and analyzed with an Analysis of Variance (ANOVA) to determine the main effects and their interactions with respect to part density. From this data, parameter sets will be developed for different locations within the determined processing window. Tensile bars in the vertical and horizontal directions with be built with the developed parameter sets and tested. Finally, micrographs in the XY and Z direction will be analyzed for each parameter set. From this data, the region on minimal energy input will be determined and mechanical properties will be compared to the rest of the processing window.

3 STATEMENT OF OBJECTIVES

The objective of these experiments was to validate the hypothesis that machine parameters for 304L stainless steel that achieve full density can be determined and optimized in the region of minimal required energy input by determining the effects of machine parameters statistically.

4 EXPERIMENTAL

4.1 POWDER

Powder was supplied by LPW Technology. Based on the findings of Section 1.3, the following requirements were given for the material; +15/-45 μm diameter powder, having a log normal distribution, and an average circularity of .8 or better. The powder was also required to meet the ASTM A240 standard for 304L.

4.2 LASER PROFILING

An Ophir camera profiler with BeamGage software was used to determine the laser beam size per the factory installation procedure. D%pk values were determined in the X and Y directions where D%pk is defined as the $\frac{1}{e^2}$ value or diameter out to 13.5% of the peak power. Laser output power was also determined by power meter per the factory installation procedure.

4.3 SINGLE LINE PROCESSING WINDOWS

Single line experiments were performed on a thin 304L substraight. This allowed for easy cross sectioning of the single line scans and a flatter surface than available on standard build plates. Drawings for the substraight and leveling hardware can be found in Appendix A. This substraight was positioned on four leveling pegs that utilize the existing bolt holes in the base plate. When the substraight was positioned on the pegs, a small screwdriver was used adjust the pegs and level the plate. To determine how level the plate was, a dial indicator was attached to the recoater and ran across the plate. To set

the correct layer thickness feeler stock was used between the recoater and the plate. A picture of the setup can be seen below in Figure 4.1.

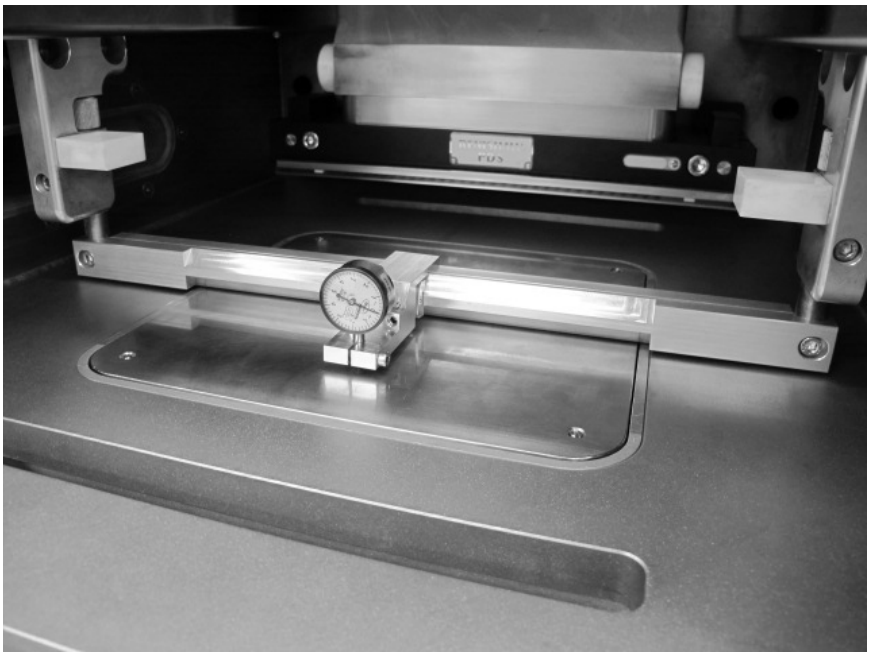

Figure 4.1: Leveling Fixture Setup Used for Single Line Scans

Build files were setup using Marcam AutoFab software. Using this software, unique exposure parameters were assigned to each part. For this experiment set, three machine parameters were varied. The parameters were laser power, exposure time, and point distance. The range of machine parameters was determined by machine limitations, supplied parameters for similar limitations, and parameters found in literature. Two builds were created, Build 1 varying laser power and exposure time with a constant point distance, and Build 2 varying laser power and point distance with a constant exposure

time. At each parameter combination, three single line scans approximately 5mm in length were made. The combinations and their identification numbers for Single Line Build 1 and Build 2 can be seen in Tables 4.1 and 4.2, respectively.

Table 4.1: Single Line Scan Build 1 Layout

Power (W)						
200	1.31	1.32	1.33	1.34	1.35	1.36
170	1.25	1.26	1.27	1.28	1.29	1.30
140	1.19	1.20	1.21	1.22	1.23	1.24
110	1.13	1.14	1.15	1.16	1.17	1.18
80	1.7	1.8	1.9	1.10	1.11	1.12
50	1.1	1.2	1.3	1.4	1.5	1.6
Exposure Time (µsec)	**50**	**100**	**150**	**200**	**250**	**300**

Table 4.2: Single Line Scan Build 2 Layout

Power (W)						
200	2.31	2.32	2.33	2.34	2.35	2.36
170	2.25	2.26	2.27	2.28	2.29	2.30
140	2.19	2.20	2.21	2.22	2.23	2.24
110	2.13	2.14	2.15	2.16	2.17	2.18
80	2.7	2.8	2.9	2.10	2.11	2.12
50	2.1	2.2	2.3	2.4	2.5	2.6
Point Distance (µm)	**25**	**50**	**75**	**100**	**125**	**150**

Once the builds were completed, the substraight was cut by bandsaw into smaller sections. Top view images and measurements were taken with A Keyence VHX-100K digital microscope. The samples were then mounted in epoxy, ground, polished, and etched with 60-40 Nitric Acid. Images and measurements of the mounted samples were then taken with a Leica DMI5000M Microscope.

4.4 DENSITY CUBES

A three level, four factor DOE was developed to investigate the effects of machine parameters on final part density. The four factors used were laser power, point distance, exposure time, and hatch spacing. The build file was created using AutoFab.

The density sample was a 1.25 cm cube at a 45° angle to the build plate. An image of the build can be seen in Figure 4.2.

Figure 4.2: Density Cube DOE Build Layout

This orientation was chosen to allow the samples to be removed by hand from the plate and to eliminate the effect of a machined surface on density determination. The first design iteration varied laser power from 50 watts to 200 watts. This range proved to be too large as the 50 watt parts where extremely porous and made the build difficult to complete without a machine crash. The DOE was redesigned for the laser power range to 100 watts to 200 watts with all other factor ranges remained the same. Three replicates of this build were produced. The factor levels chosen were similar to the single line scans,

but their range was reduced to ensure successful builds. The values used can be seen in Table 4.3.

Table 4.3: 3 Level DOE Values

Factor Level	Value
P-	100 W
P0	150 W
P+	200 W
PD-	52.5 μm
PD0	70 μm
PD+	87.5 μm
ET-	120 μsec
ET0	150 μsec
ET+	180 μsec
HS-	52.5 μm
HS0	70 μm
HS+	87.5 μm

The cubes were removed from the plate either by hand or with the use of chisel and hammer. Mass for the cubes was taken using an Ohaus Explorer 324 scale. Volume was then determined by Helium Pycnometry utilizing a Micromeritics AccuPyc1340

where each sample was exposed to ten, 19.5 PSI purge cycles before a reading was taken. From these values, density was calculated.

4.4.1 Density Measurement Comparison. In addition to helium pycnometry, several other methods were used to determine density. Four replicates of three samples were chosen representing a range of energy densities and each replicate was used to test a different method of density determination. The samples tested appeared to be water tight from a visual inspection of the outside surface and this was confirmed by the micrographs used for optical determination. A full summary of the results is found in Figure 4.4.

In addition to helium pycnometry, Archimedes' method per ASTM B962 in water and isopropyl alcohol was performed. The findings of Spierings et al. [60] showed Archimedes' method for watertight samples to be the most accurate and repeatable of the tested methods. The study performed by Spierings et al. did not including helium pycnometry. Results found in Figure 4.4 are in agreement with Spierings where isopropyl alcohol is the preferred media for Archimedes' method. From these results, it can be concluded that with the constraint of the samples being watertight, helium pycnometry is a preferable alternative to Archimedes' method as results are comparable to those determined using alcohol. Helium pycnometry also has the advantage that it is a more automated and removes some of the possible human error.

Density was also determined by an optical method. To determine density by this method, the samples were sectioned, mounted, ground, and polished. A macro image was then taken with a Lecia DFC290 camera and the image was then processed using MATLAB. A program was written to convert the image to grayscale, crop the image, threshold the image, remove noise, and finally determine the area difference between

black and white pixels. This color difference was recognized and density is calculated. The progression of image processing is found in Figure 4.3.

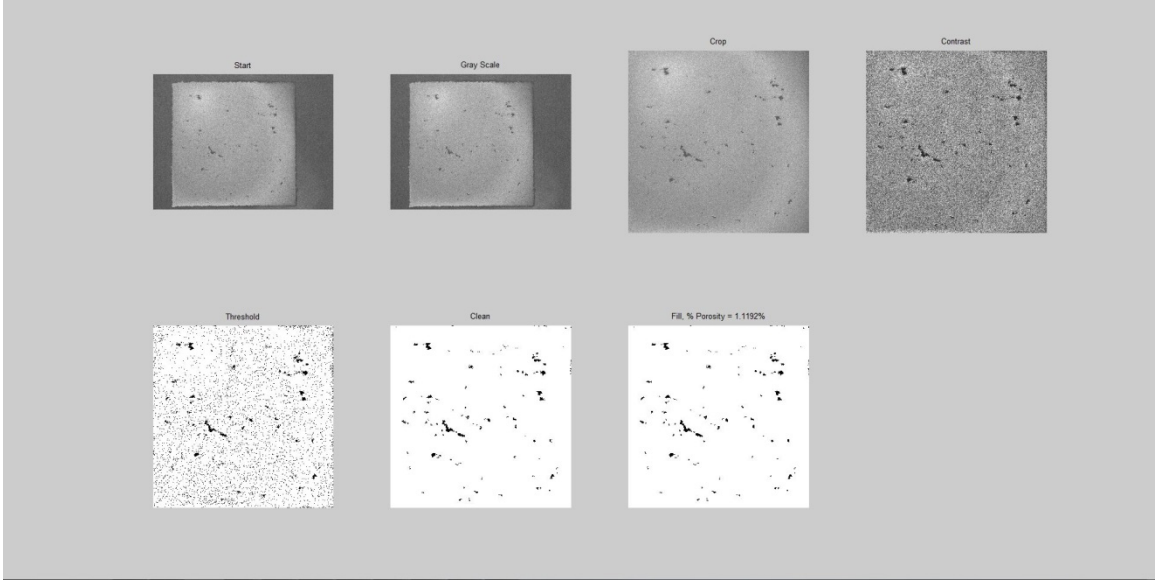

Figure 4.3: MATLAB Image Processing Progression for a Single Sample

In comparison to the other methods, it can be seen that the optical method consistently returns higher values than the other tested methods. Because only one image was taken, the error for the density is potentially high and with only a single image porosity can either be high or low, depending on the distribution of pores on the layer imaged. With this taken into consideration and accounted for, although more labor intensive and less accurate, for samples that have open porosity and are no longer watertight, this method can be used as an alternative. Although labor intensive, optical is

still be a preferred method than the alternative of encapsulating parts before performing Archimedies' method.

For these three samples, open and closed porosity amounts were calculated. Porosity was determined by calculating the skeletal volume and taking the dry and wet masses. Wet mass was determined by submerging the samples in boiling water, allowing the water to fully penetrate the part. The part was then removed from the water and any excess water on the surface was removed. It can be seen for the three samples, open porosity remained constant where closed porosity increased as energy density increased. This follows the trends shown that as energy density increases beyond the apparent cusp, part density decreases. The constant open porosity further indicates watertight parts.

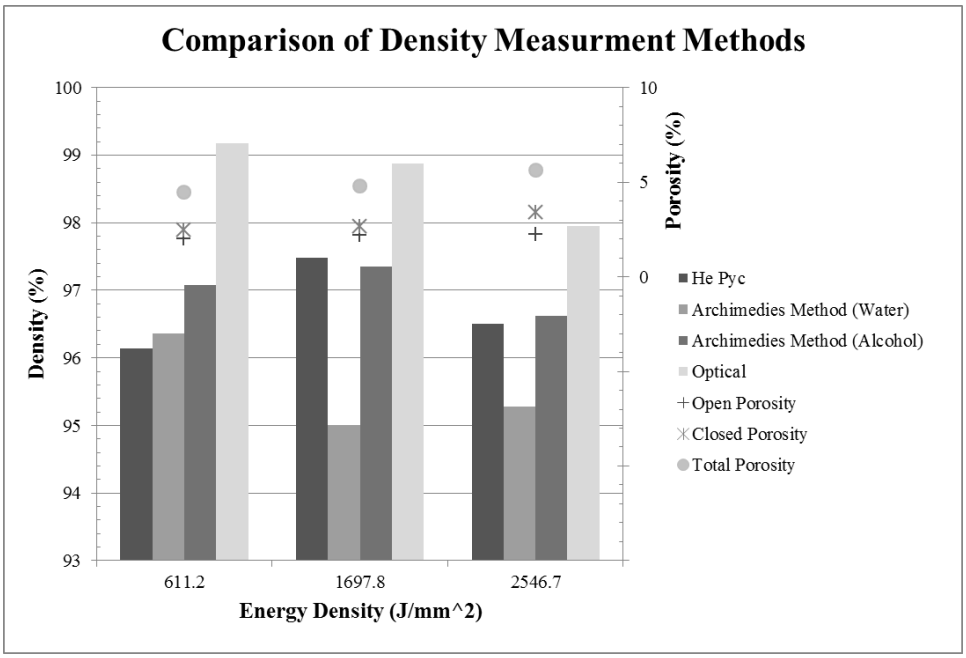

Figure 4.4: Comparison of Density Measurement Methods

4.5 OPTIMIZED PARAMETER SET TESTING

From the results of the single line and density cube DOE, parameter sets of decreasing energy density were created. The build file was again created in AutoFab. For each of the ten parameter sets three vertical and three horizontal tensile bar blanks were built, as well as a density cube. The setup for the build can be seen in Figure 4.5. Each blank was a 9 mm diameter cylinder approximately 45 mm in length. The blanks were then machined to a R4 tensile bar per ASTM E8. A drawing of the bar designed used can be seen in Figure 4.6. Tensile samples were machine and tested per ASTM E 8, and density cubes analyzed by helium pycnometry. After density was determined, the cubes were sectioned, mounted, and polished. Macro images were taken using a Lecia DFC290 camera. The samples were then etched using 60-40 Nitric Acid and micrographs were taken using a Lecia DMI5000M Microscope.

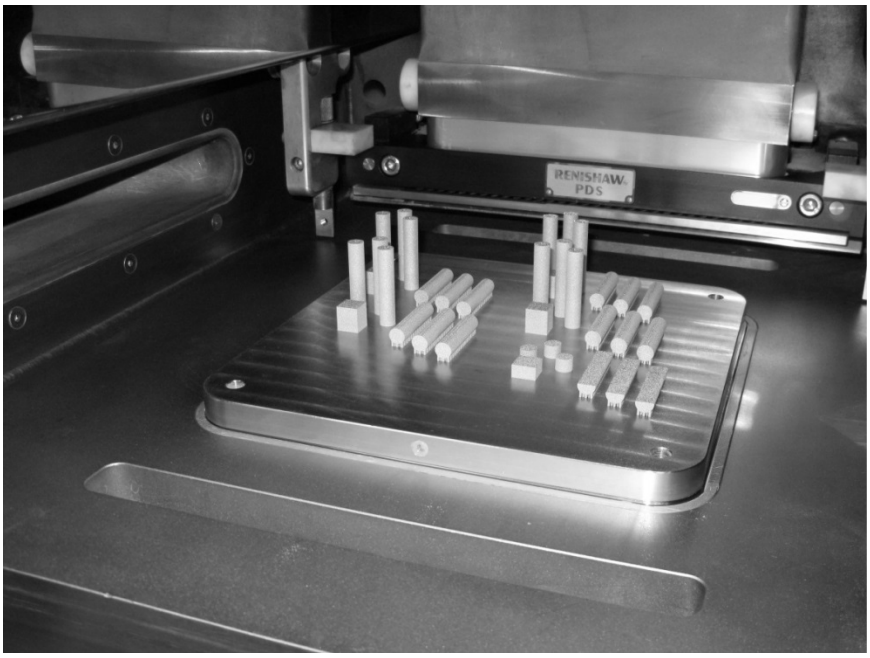

Figure 4.5: Optimized Parameter Set Build Layout With One Failed Parameter Set

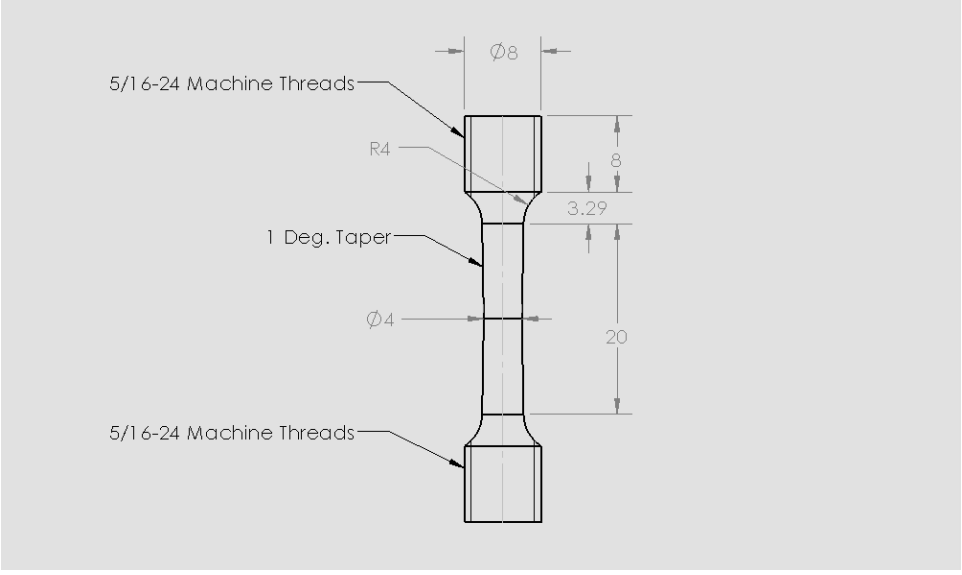

Figure 4.6: R4 Tensile Bar Design Used for Tensile Study

4.6 ENERGY INPUT QUANTIFICATION

For the scan pattern used by the AM250, none of the existing power or energy density terms discussed in Section 1.2.2 accurately quantifies the machine parameters. Because of this, a new term needed to be formulated. Starting with the power density of a single point and multiplying by exposure time, an energy density for a single point can be determined. This is seen in Equation 7. From this formula the point and hatch overlaps need to be taken into account. These ratios can be seen in equations 8 and 9, respectively.

$$E_{\rho 1} = \frac{P}{ss} \cdot et \tag{7}$$

$$Point\ Overlap = \frac{x_1}{pd} \tag{8}$$

$$Hatch\ Overlap = \frac{x_2}{hs} \tag{9}$$

Taking equations 6 through 8 and multiplying them together results in a specific energy bdensity per unit area. This final formulation can be seen in equation 10. This formulation does not attempt to take any losses into account and is merely used to quantify machine parameters into an energy input term in units of $\frac{\mathrm{J}}{\mathrm{mm}^2}$.

$$E_{\rho 2} = \frac{P}{ss \cdot hs \cdot pd} \cdot et \tag{10}$$

5 RESULTS AND DISCUSSION

5.1 POWDER ANALYSIS

5.1.1 Sizing and Distribution. Size and morphology analysis was performed by Malvern Instruments UK using a Morphologi G3. The Morphologi G3 performs static image analysis and then processes the images to determine the samples size and morphology distributions. 100,429 particles were analyzed and results show that the material has a log-normal distribution between ranging between approximately 5μm and 100μm. The distribution plot can be seen in Figure 5.1.

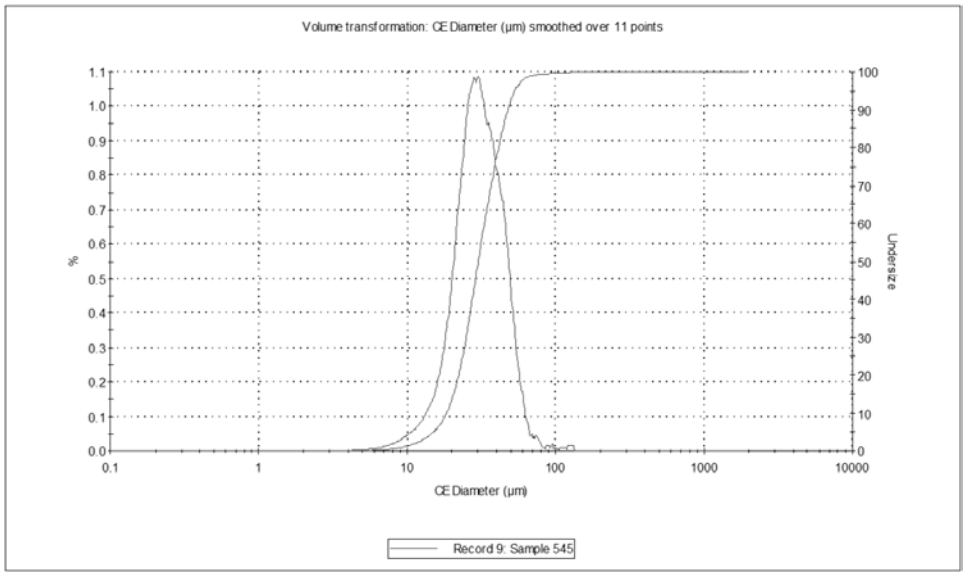

Figure 5.1: Particle Size Distribution Determined by a Morphologi G3 and Supplied by LPW

Morphology analysis was conducted and the results in the vicinity of the 10th, 50th, and 90th percentile for size were reported and values were found to be approximately 9.75µm, 30.5µm, and 61µm, respectively. Results can be seen in Figures 5.2-5.4. Although the material was sieved between 15 µm and 45 µm, some particles outside of this range are present in the material. However, as shown by the D10 and D90 values, most particles are within a distribution close to the sived values. The D10 value below 10 µm lead to some pluming of powder where some particles became airborne when being worked with, but no issues with agglomeration or flowability were noticed.

It can be seen that the particles become less spherical as size increases, but still remaining close to the .8 or better circularity requirement. SEM images at the magnifications of x100, x500, and x1000 were also taken and can be seen in Figures 5.5-5.7 respectively. In these images, the distribution of size and shape of the material can be seen more clearly.

Figure 5.2: 10th Percentile Region Powder Morphology Determined by a Morphologi G3 and Supplied by LPW

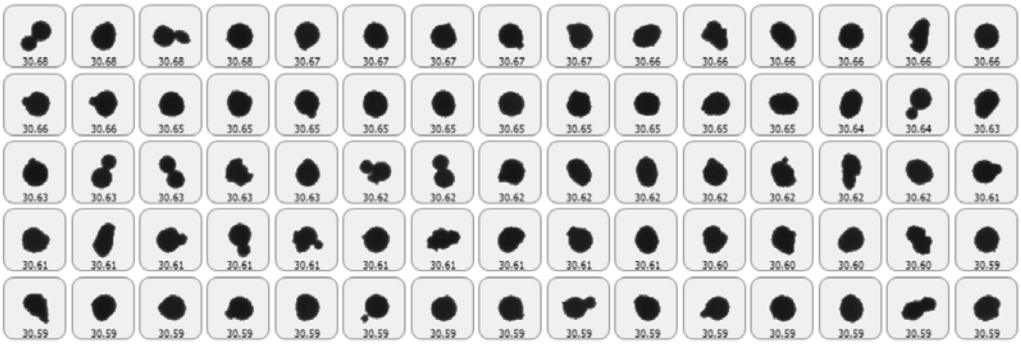

Figure 5.3: 50th Percentile Region Powder Morphology Determined by a Morphologi G3 and Supplied by LPW

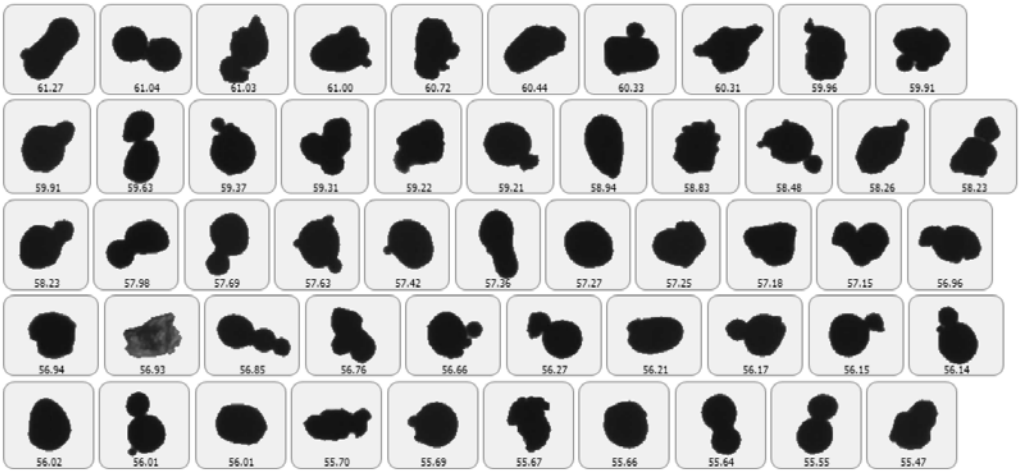

Figure 5.4: 90th Percentile Region Powder Morphology Determined by a Morphologi G3 and Supplied by LPW

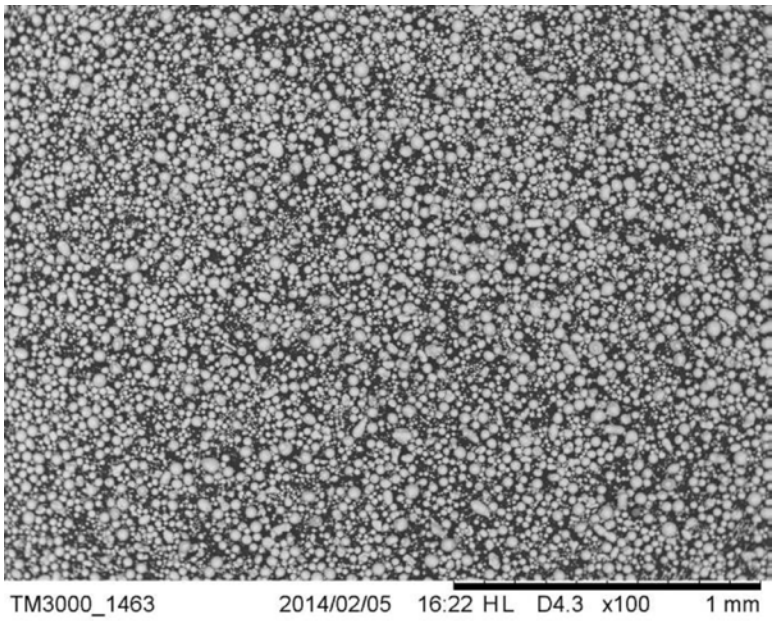

Figure 5.5: x100 Magnification SEM Image Supplied by LPW

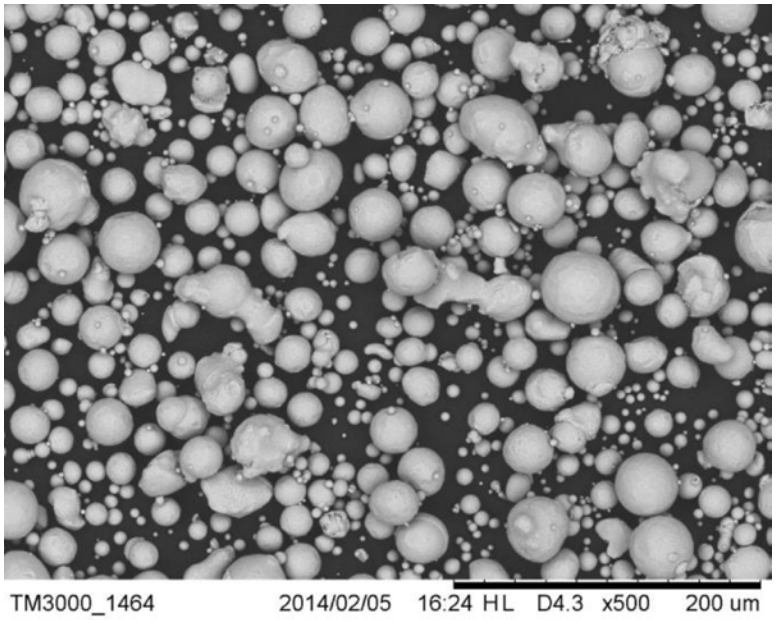

Figure 5.6: x500 Magnification SEM Image Supplied by LPW

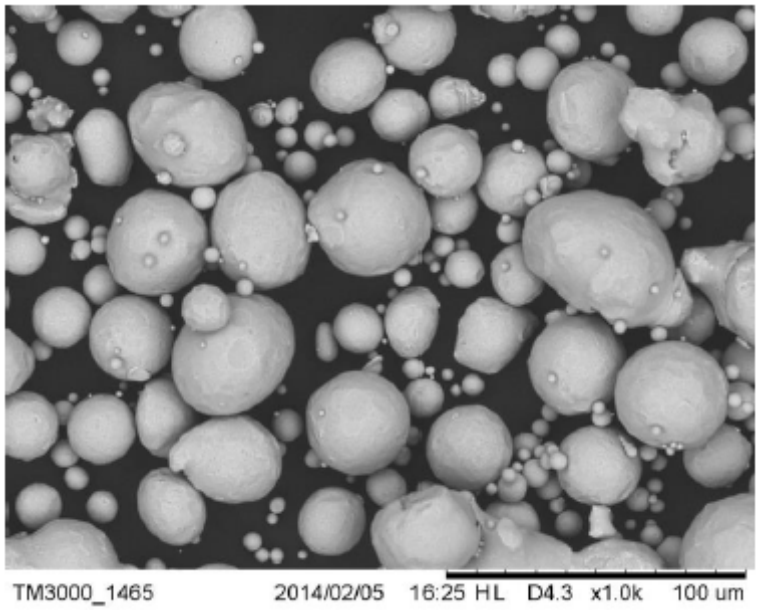

Figure 5.7: x1000 Magnification SEM Image Supplied by LPW

5.1.2 Tap Density and Apparent Density. Tap and apparent density of the powder was measured to help indicate flowability. Results can be seen below in Table 5.1. From these results the Hausner Ratio can be calculated to be 1.122 per Equation 6. As previously discussed, this value indicates good flowability and was seen to be true when working with the powder. A 14.9938g sample of material was taken to determine the density of the powder by Helium Pycnometry. The density of the powder was determined to be 7.9467 $\frac{g}{cm^2}$.

Table 5.1: Powder Densities

	Test 1	**Test 2**	**Test 3**
Mass (g)	100.0	100.0	100.0
Volume at Zero Taps (cm^2)	20.5	20.0	20.5
25	19.5	19.5	19.0
50	18.5	19.0	19.0
100	18.0	18.5	19.0
200	18.0	18.5	18.5
400	18.0	18.5	18.0
800	18.0	18.5	18.0
Apparent Density $\left(\frac{g}{cm^2}\right)$	4.9	5.0	4.9
Tapped Density $\left(\frac{g}{cm^2}\right)$	5.6	5.4	5.6
Average Apparent Density $\left(\frac{g}{cm^2}\right)$	4.9		
Average Tapped Density $\left(\frac{g}{cm^2}\right)$	5.5		
Skeletal Density $\left(\frac{g}{cm^2}\right)$	7.9467		

5.1.3 Chemistry. Chemistry was tested at the supplier by inductively coupled plasma-atomic emission spectroscopy and the weight percent values and the comparison to the ASTM A240 standard can be seen below in Table 5.2 as meeting the standard for Type 304L Stainless Steel.

Table 5.2: Powder Chemistry Comparison

	ASTM A240 Type 304L wt%	Actual wt%
Carbon	.03 Max	0.013
Manganese	2.00 Max	1.38
Phosphorus	0.045 Max	0.009
Sulfur	0.030 Max	0.008
Silicon	0.75 Max	0.55
Chromium	17.5-19.5	18.9
Nickel	8.00-12.00	9.9
Nitrogen	0.10 Max	0.09
Iron	Balance	Balance

5.2 LASER PROFILING

Laser power and beam size as measured at the time of machine installation can be seen in Table 5.3. A constant focal offset determined during factory installation was used for all powers.

Table 5.3: Laser Profile at Various Powers

Apparent Laser Power	Actual Laser Power	D%pkx	D%pky	Focal Offset
200 W	194 W	67.8 µm	68.4 µm	-3.5 mm
150 W	147 W	66.0 µm	66.4 µm	-3.5 mm
100 W	97 W	66.3 µm	67.9 µm	-3.5 mm
50 W	48 W	66.9 µm	68.7 µm	-3.5 mm

5.3 SINGLE LINE EXPERIMENTS

5.3.1 Processing Window. In order to combine Build 1 and Build 2 where different parameters were varied into a single window, point distance and exposure time were combined into a speed term according to the formulation in Equation 11.

$$Speed = \frac{Point\ Distance}{Exposure\ Time} \tag{11}$$

This combination of terms was considered after reviewing the Main Effect Plots created in MiniTab using the width and depth measurements of the scans. These plots for width and depth can be seen in Figures 5.8 and 5.9, respectively.

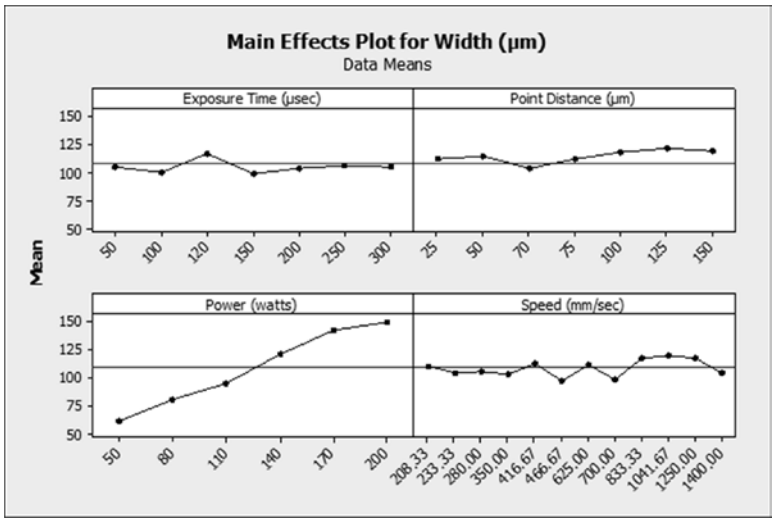

Figure 5.8: Single Line Scan Build 1 and Build 2 Main Effects for Width

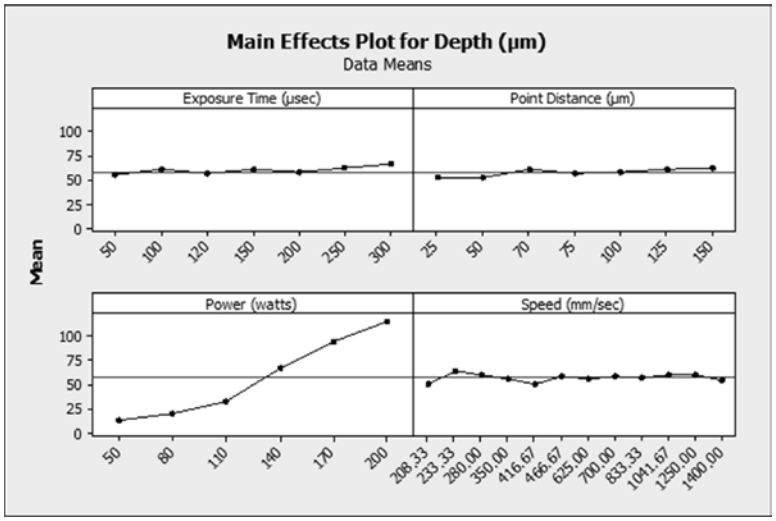

Figure 5.9: Single Line Scan Build 1 and Build 2 Main Effects for Width

Both exposure time and point distance have no significant effect on single line geometry over the range tested in Build1 and Build 2. However, power has a clear effect on geometry. This is similar to the findings by Averyanova et al. [10] where for one of the powder distributions tested, power had the main effect on single line geometry. Speed was formulated and its effect can also be seen in Figures 5.8 and 5.9 to have no effect on geometry over the range tested in Build 1 and Build 2. With this combination of parameters a processing window was made and can be seen in Figure 5.10. The processing window identifies the sample with the first number depicting the Build number and the second number depicting the individual parameter set number per Tables 4.1 and 4.2 found in Section 4.3.

Power (W)												
200	2.31	1.36	1.35 ●	1.34	2.32 ●	1.33	2.33	1.32	2.34	2.35	2.36	1.31
170	2.25	1.30	1.29	1.28	2.26	1.27	2.27	1.26	2.28	2.29	2.30	1.25
140	2.19	1.24	1.23	1.22	2.2	1.21	2.21	1.20	2.22	2.23	2.24	1.19
110	2.13 *	1.18 *	1.17 *	1.16 *	2.14 *	1.15 *	2.15 *	1.14 *	2.16 *	2.17 *	2.18 *	1.13 *
80	2.7 * +	1.12 * +	1.11 *	1.10 *	2.8 *	1.9 *	2.9 *	1.8 *	2.10 *	2.11 *	2.12 *	1.7 * +
50	2.1 * +	1.6 * +	1.5 * +	1.4 * +	2.2 *	1.3 *	2.3 *	1.2 *	2.4 * +	2.5 * +	2.6 * +	1.1 * +
Speed (mm/s)	**208**	**233**	**280**	**350**	**417**	**467**	**625**	**700**	**833**	**1042**	**1250**	**1400**
● Porosity *Penetration < 50μm + Incomplete Melt												

Figure 5.10: Processing Window Developed From Single Line Scans

The developed processing window denotes several regions where the processing conditions created failed scan track. Combinations denoted by the asterisk (*) exhibited melt pool penetration less than 50 µm. This is undesirable as this penetration is at or below the set layer thickness of 50 µm and this can lead to layer separation in a build. Two other regions denoted by a plus (+) exhibit incomplete melt. These regions were found at low power levels at both the high and low speed extremes. Both of these regions appeared to have the same incomplete melt appearance and no clear indication of balling or over energizing could be seen. These failure regions appear to be a result of too low of an energy input.

As denoted in the processing window by a circle (●), porosity was found in a total of two samples. As shown by King et al. [45], keyhole mode melting in the SLM process can lead to the collapsing of the created vapor column leaving porosity. In the first set of images, porosity was only found in 1 scan track of sample 1.35. Upon re grinding, samples 2.31, 1.36, 1.35, 1.34, 2.32, 2.25, 1.30, 1.29, 1.28, and 2.26, another pore was found in a single line of sample 2.32. Both samples that contained porosity we found in the low speed range of the processing window. This corroborates the findings of Monroy et al. [22] that at lower speeds pores form and are larger due to retained heat. An effort was made to increase the number of point that images were taken, only two samples with porosity were found. However, it can be assumed that other samples in the high power and low speed region also contain porosity. Although there is no clear visual indication from the top surface as seen in other processing windows in literature, this still follows the same trend of a region at high power and low speed being over energized.

Selected top and cross section view images from across the processing window can be found in the following section.

The data for laser power's effect on geometry in Build 1 can be found in Figures 5.11 and 5.12 for width and depth, respectively. Data for Build 2 can be found in Figures 5.13 and 5.14. Regression equations were found to predict single track width and depth as a function of laser power. Plots can be found in Figures 5.15 and 5.16. From the predictions seen in Figures 5.15 and 5.16, geometry limitations can be implemented on parameter sets.

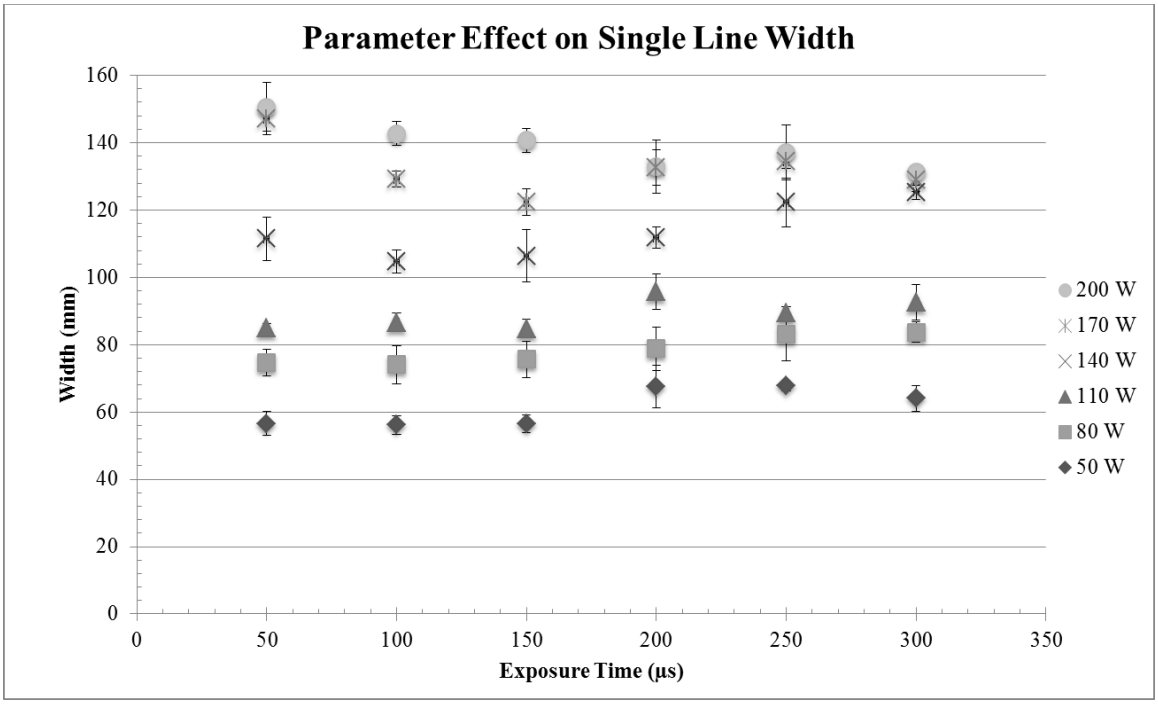

Figure 5.11: Build Parameter Effect on Width

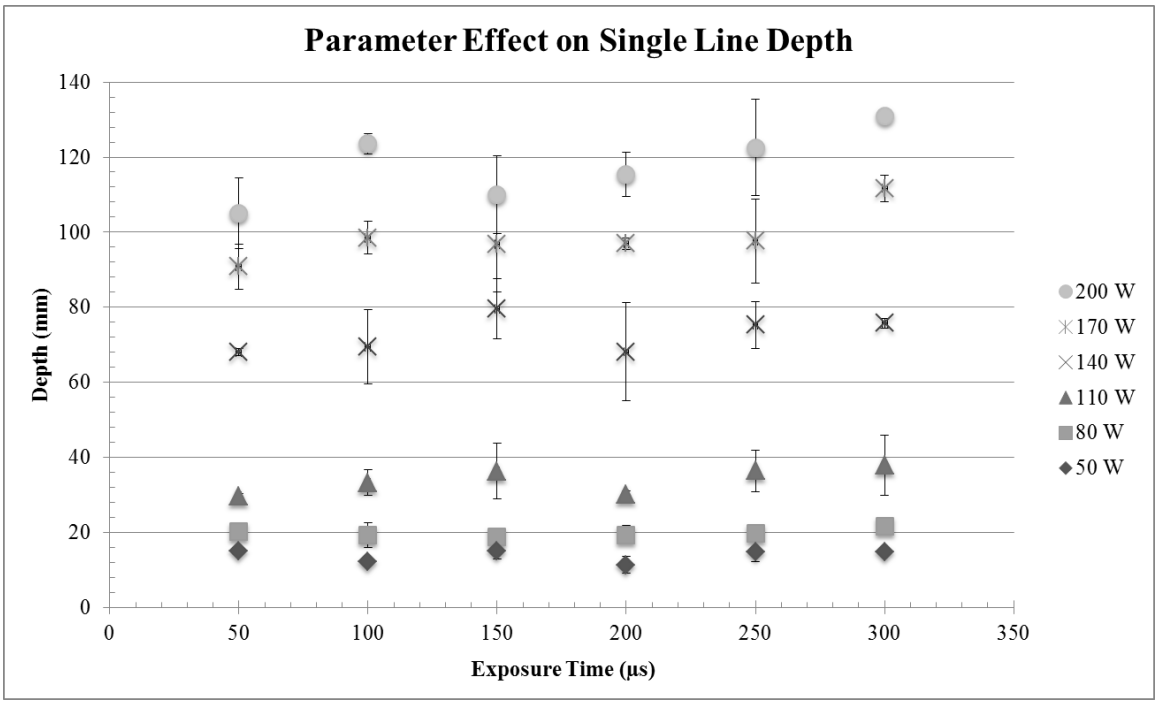

Figure 5.12: Build 1 Parameter Effect on Depth

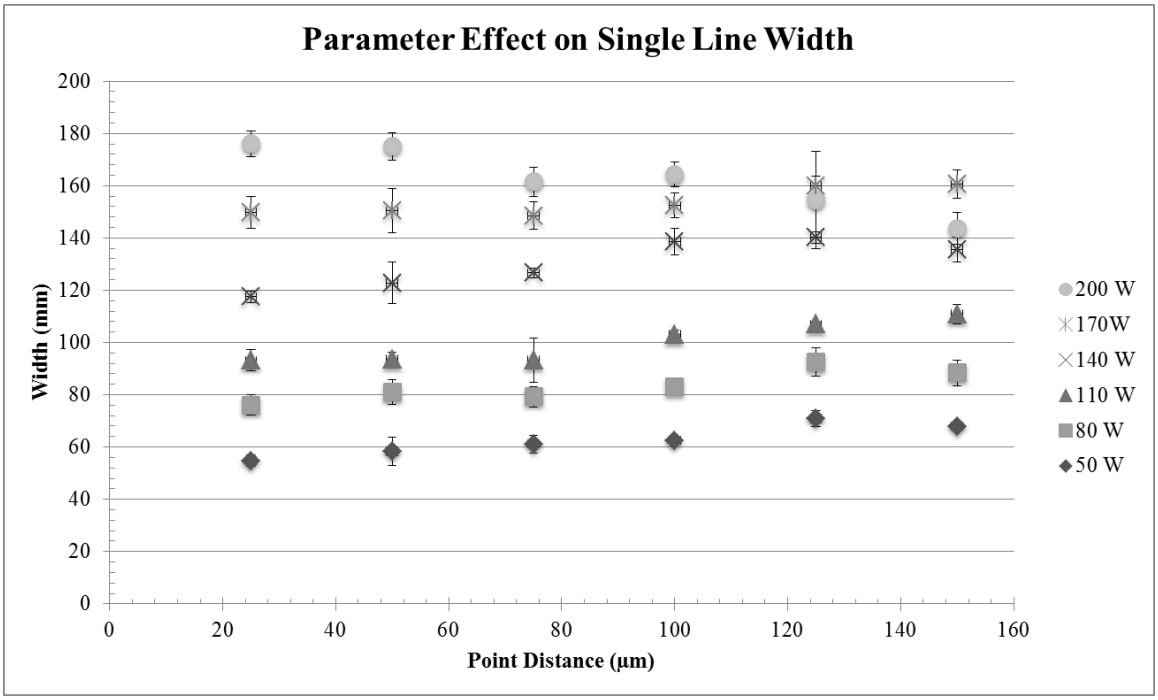

Figure 5.13: Build 2 Parameter Effect on Width

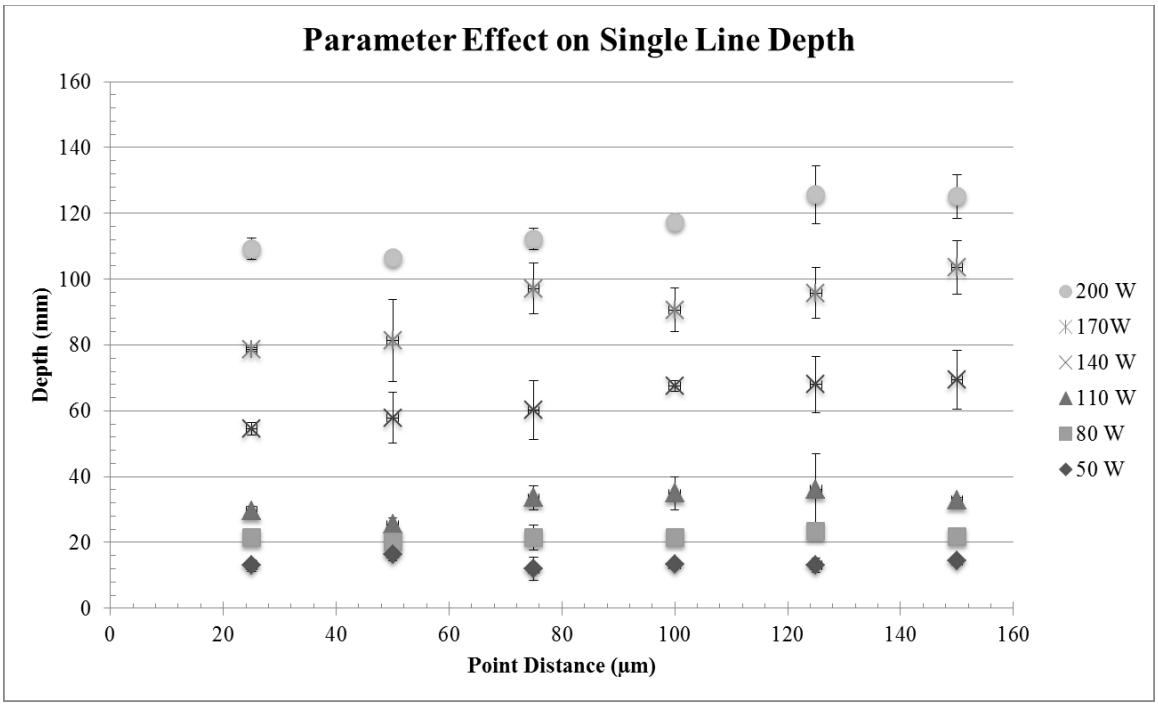

Figure 5.14: Build 2 Parameter Effect on Depth

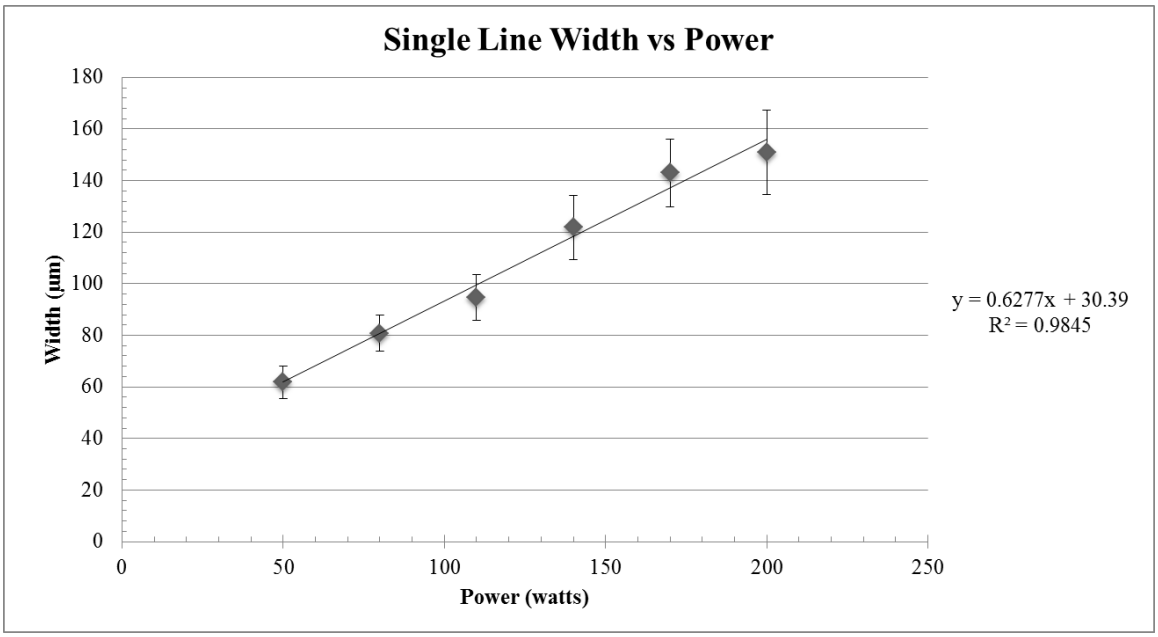

Figure 5.15: Best Fit for Width

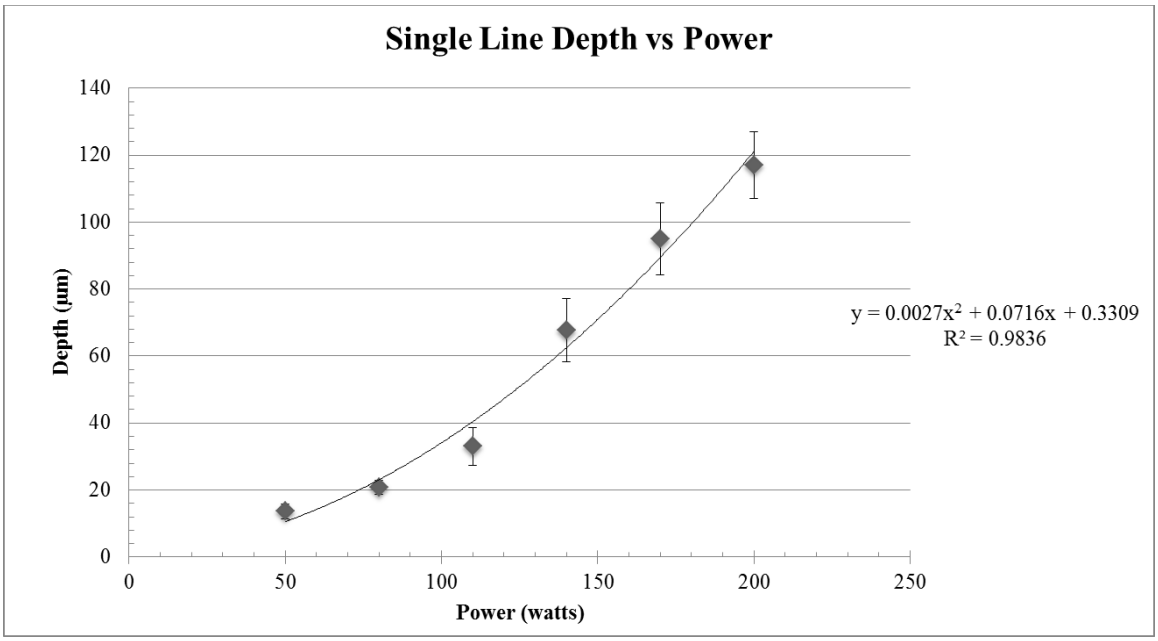

Figure 5.16: Best Fit for Depth

5.3.2 Micrographs. Images from eight difference parameter sets can be seen in Figures 5.17-5.32. The appearance of the top surface as well as the cross section was used to develop a processing window. Images of the pores found in samples 1.35 and 2.32 can be found in Figures 5.33 and 5.34, respectively.

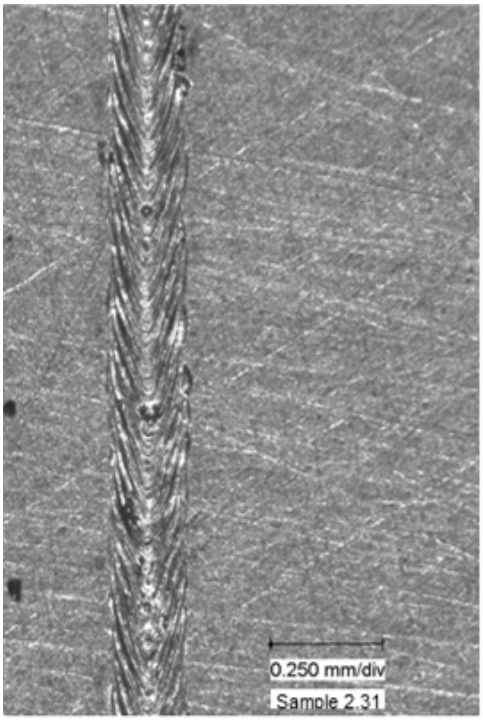

Figure 5.17: Sample 2.31 Top View

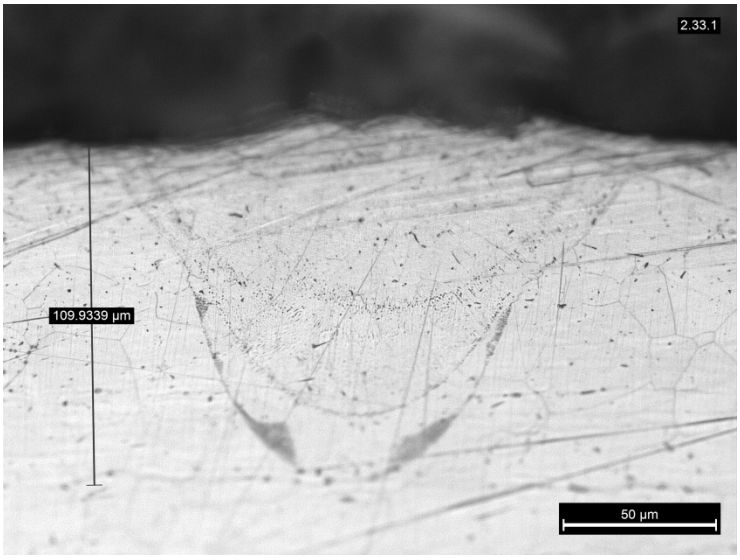

Figure 5.18: Sample 2.31 Cross Section View

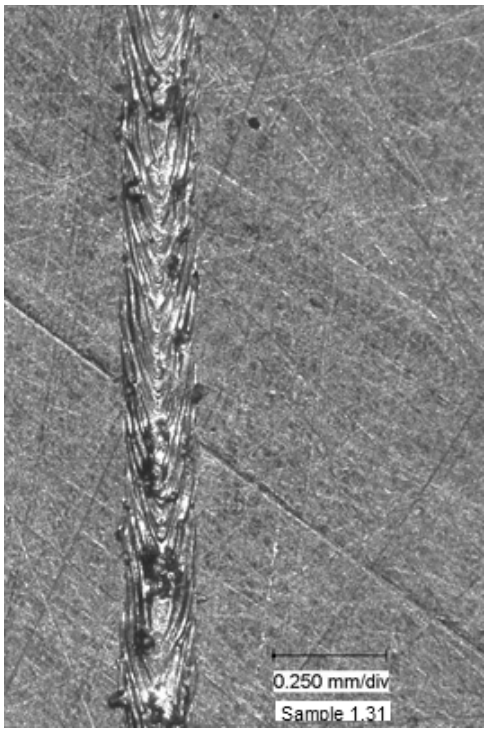

Figure 5.19: Sample 1.31 Top View

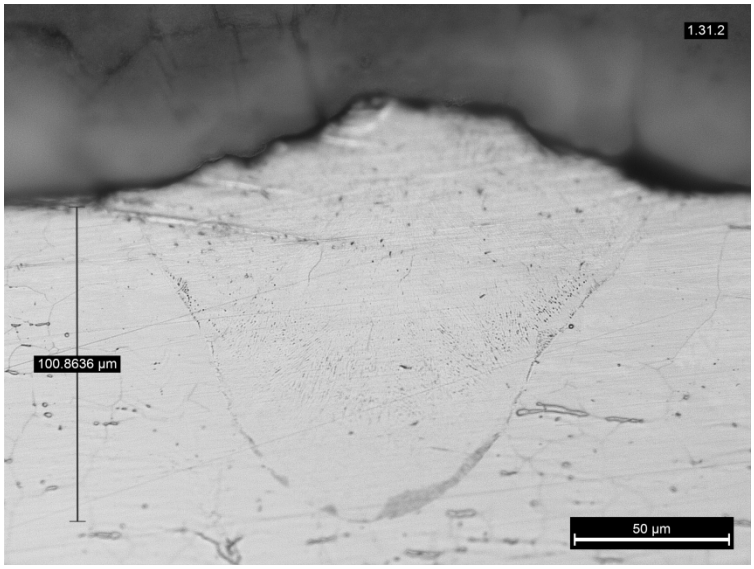

Figure 5.20: Sample 1.31 Cross Section View

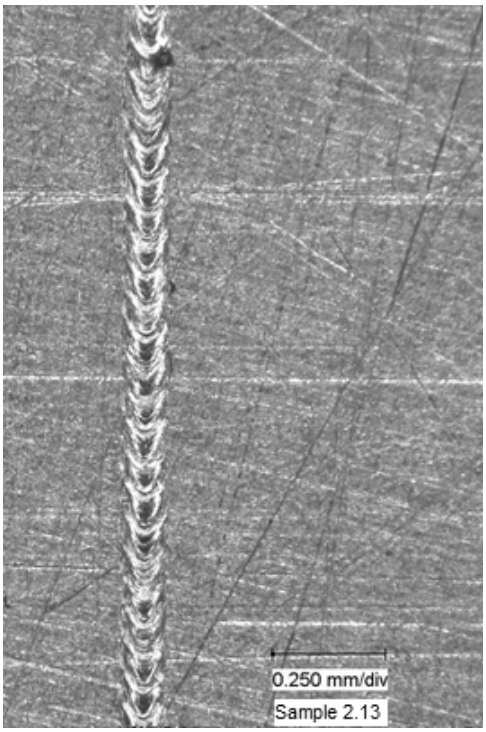

Figure 5.21: Sample 2.13 Top View

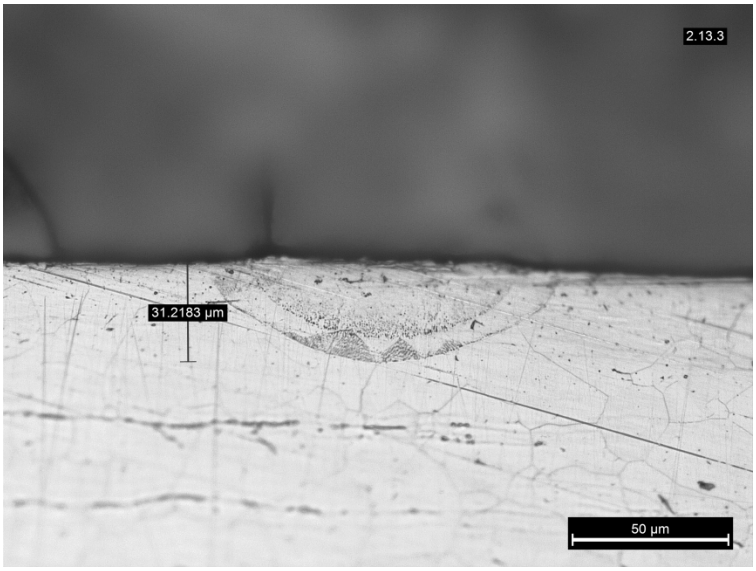

Figure 5.22: Sample 2.13 Cross Section View

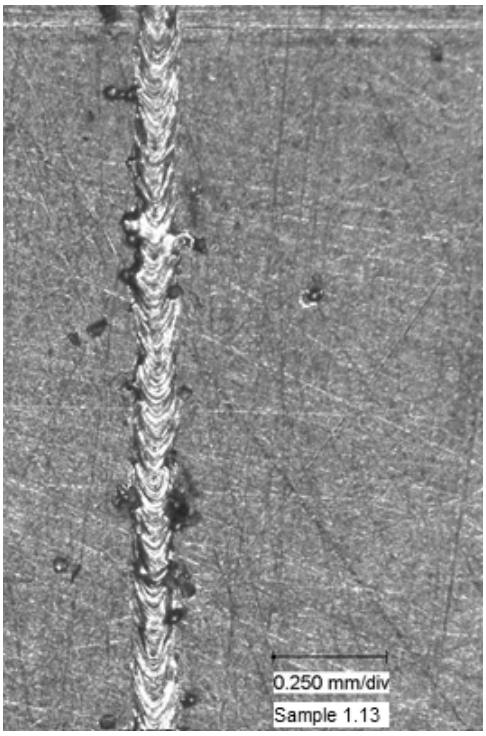

Figure 5.23: Sample 1.13 Top View

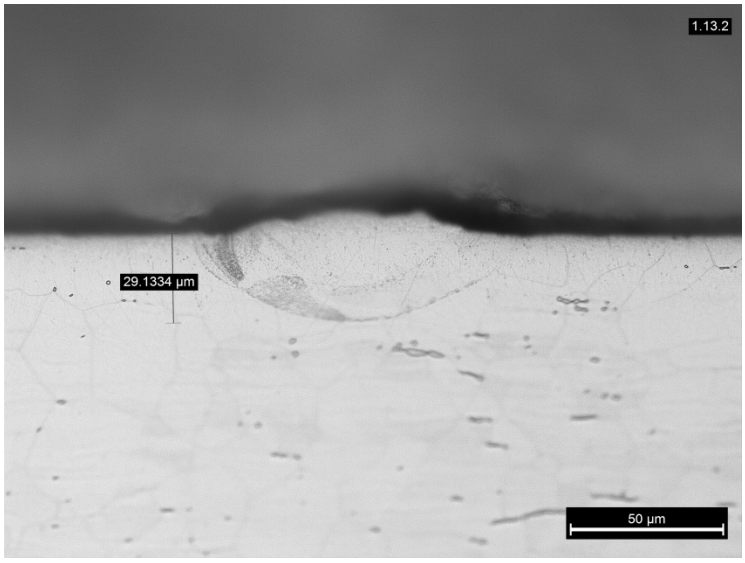

Figure 5.24: Sample 1.13 Cross Section View

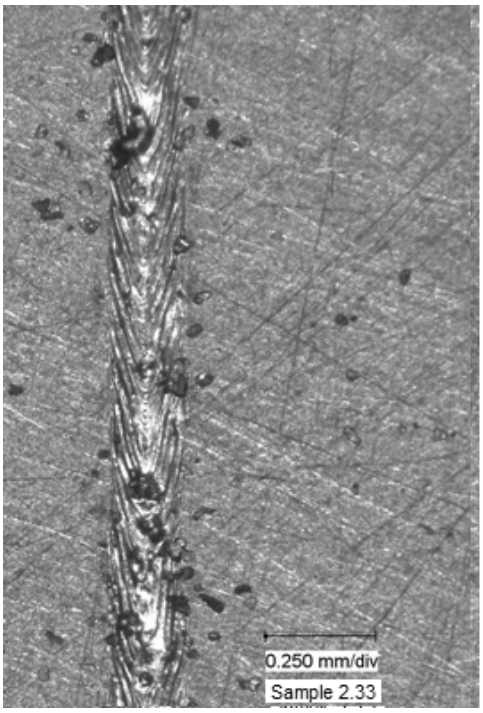

Figure 5.25: Sample 2.33 Top View

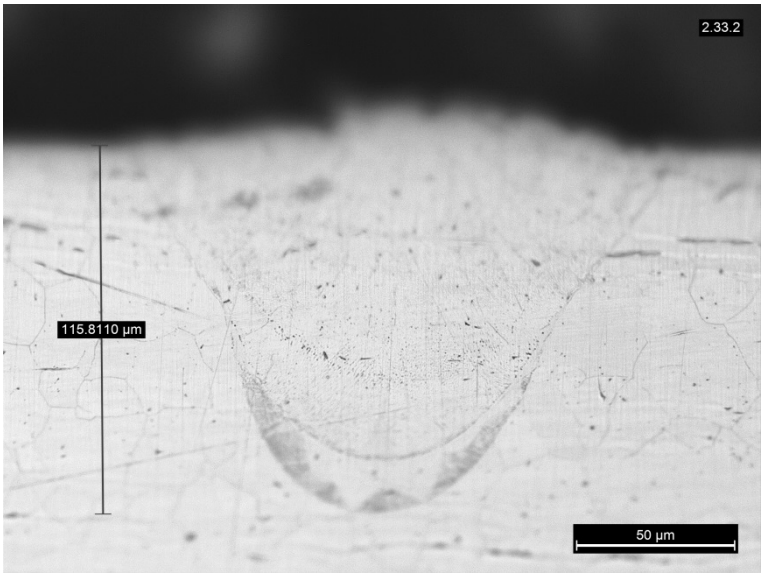

Figure 5.26: Sample 2.33 Cross Section View

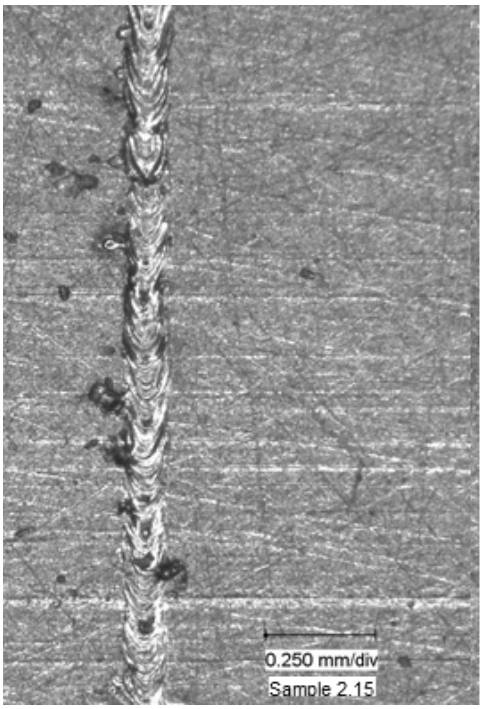

Figure 5.27: Sample 2.15 Top View

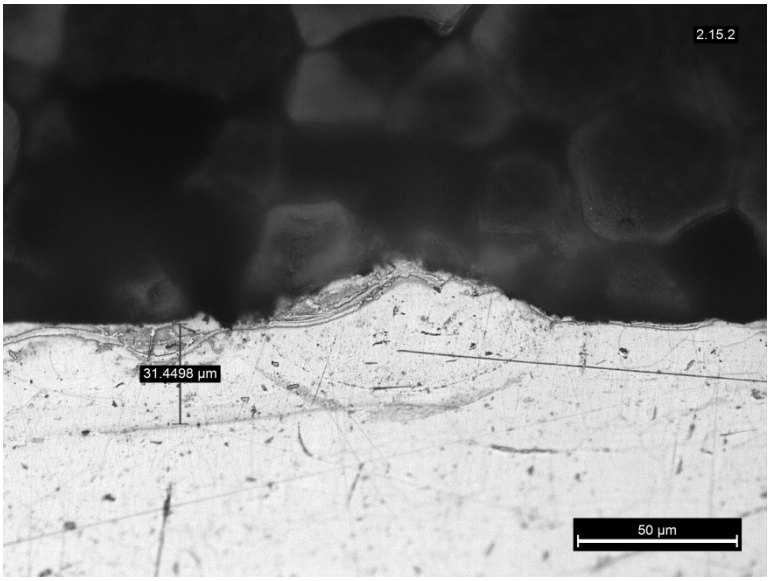

Figure 5.28: Sample 2.15 Cross Section View

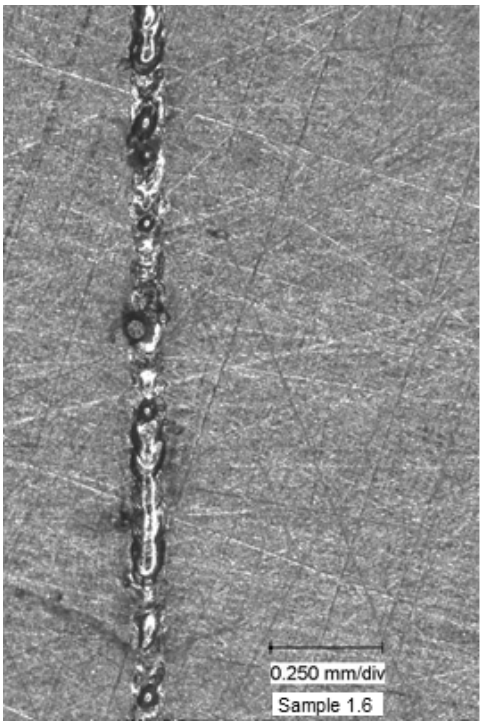

Figure 5.29: Sample 1.6 Top View

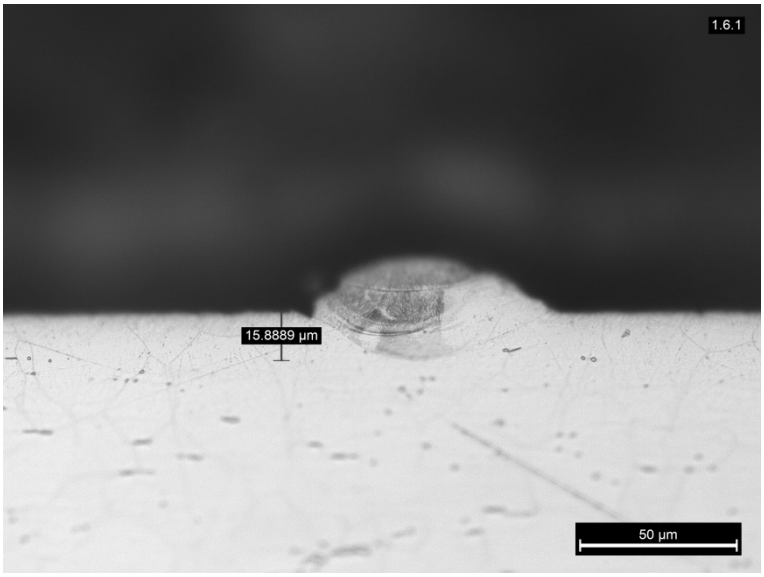

Figure 5.30: Sample 1.6 Cross Section View

Figure 5.31: Sample 2.6 Top View Top View

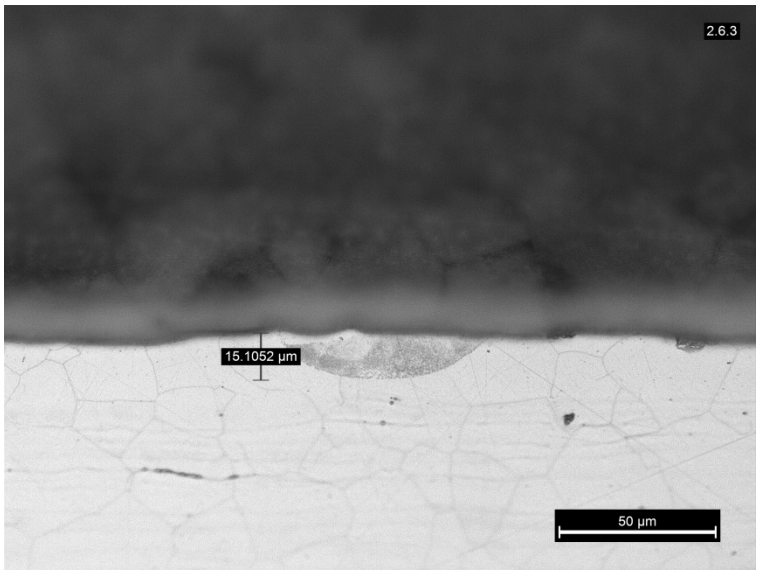

Figure 5.32: Sample 2.6 Cross Section View

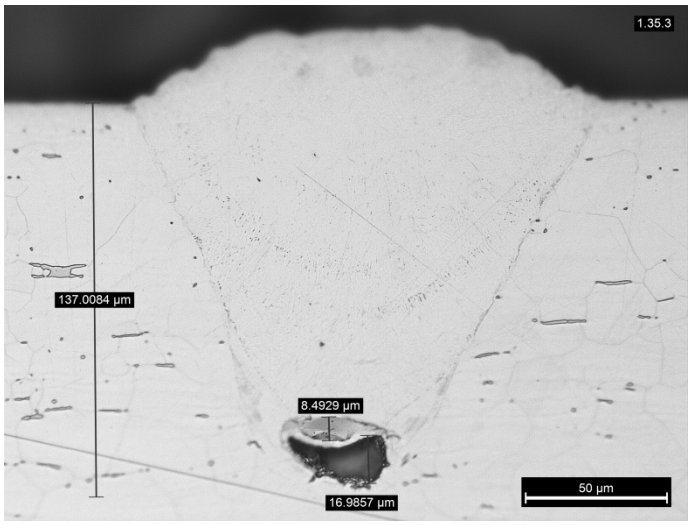

Figure 5.33: Pore Found in Sample 1.35

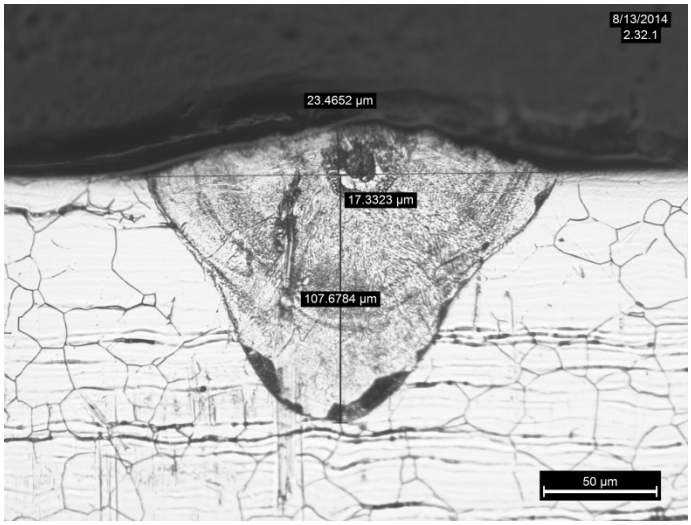

Figure 5.34: Pore Found in Sample 2.32

5.4 DENSITY CUBES

Three lots of 81 cubes each were built and one full lot of 81 cubes was initially evaluated. Each cube was broken off the build plate following build completion. Three

levels where initially chosen to determine if the parts exhibited linear responses to parameter change. Varying of hatch spacing overlap from 0% to 50% has been shown by Guan et al. [61] to have no effect on mechanical properties. However, increasing hatch spacing from 0% to +50% can have an effect where scan tracks no longer overlap and allowing for porosity in the final part. For this DOE, the nominal factor for both point distance and hatch spacing were set at 70 µm which equates to 0% overlap based on laser spot size found in Section 5.2. The range for each of these factors was then selected as ±25% of the nominal value. Data from the three level design was analyzed to determine if the three levels where required. A Main Effects Plot was generated to investigate linearity and can be seen below in Figure 5.35.

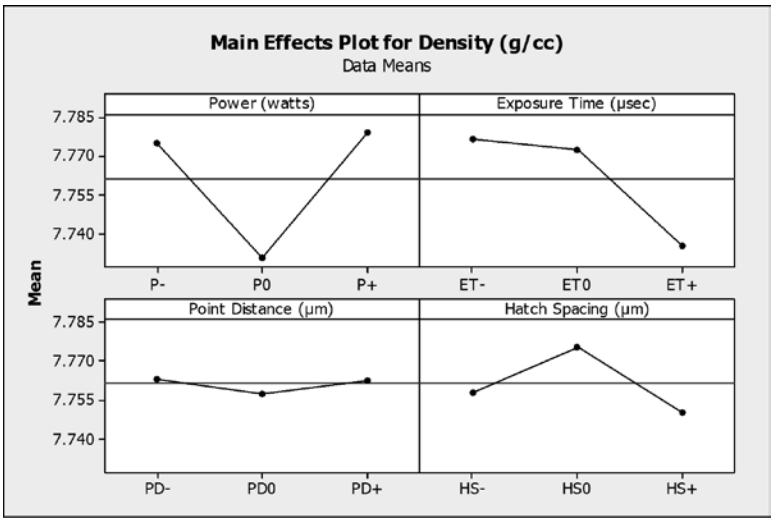

Figure 5.35: 3 Level DOE Main Effect Plots for Density

The main effects plot in Figure 5.35 shows what appears to be non-linear behavior for power and hatch spacing. However when the range is taken into consideration for hatch spacing, the behavior can be taken as linear. The nonlinear response for power was due to some outliers in the data set. From these results, over the range tested the factors exhibited a linear response for density. The Original DOE was modified to remove the nominal value, leaving only 2 levels reducing the lot size from 81 parts to 16 parts. With the redesigned DOE determined, the remaining two lots of 16 parts had their density calculated. The data from the three lots was then analyzed. A Main Effects Plot for the two level design can be seen in Figure 5.36.

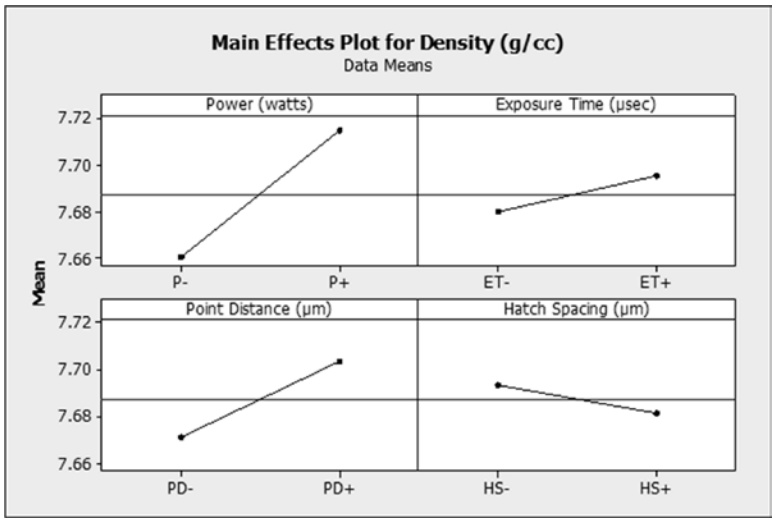

Figure 5.36: 2 Level DOE Main Effect Plots for Density

From Figure 5.36 we it can be seen that same as the single line scans, power has a significant effect. Exposure time is shown to have a slight effect. However when the scale

on the graph is kept in mind, the effect is minimal. Point distance show the effect of as it increases, so does density. This effect if further discussed later in this section. Finally, the effect of hatch spacing shows that as this factor increases, density decreases. Like the effect of exposure time, this appears to be minimal.

An ANOVA was then performed on the data to determine the statistical main effects of the factors and their interactions. The resulting ANOVA Table can be seen in Table 5.4. From these results it can be seen that Power and Point Distance, as well as the combinations of Power/Point Distance, Power/Exposure Time, Exposure Time/Point Distance, and Exposure Time/Point Distance/Hatch Spacing all have significant effect with 95% confidence on Density.

Table 5.4: DOE ANOVA

Source	DF	Seq SS	Adj SS	Adj MS	F	P
Blocks	2	0.15941	0.15941	0.079707	46.03	0.000
Main Effects	4	0.052850	0.052850	0.013213	7.63	0.000
P	1	0.035520	0.035520	0.03552	20.51	0.000
ET	1	0.002775	0.00278	0.002775	1.60	0.215
PD	1	0.012890	0.012890	0.01289	7.44	0.010
HS	1	0.00167	0.00167	0.001665	0.96	0.334
2-Way Interactions	6	0.067160	0.067160	0.011193	6.46	0.000
P*ET	1	0.02342	0.02342	0.023421	13.53	0.001
P*PD	1	0.029200	0.029200	0.029201	16.86	0.000
P*HS	1	0.00112	0.00112	0.001124	0.65	0.427
ET*PD	1	0.01207	0.01207	0.012067	6.97	0.013
ET*HS	1	0.00135	0.00135	0.001346	0.78	0.385
PD*HS	1	1E-06	1E-06	1.2E-06	0.00	0.979
3-Way Interactions	4	0.01947	0.01947	0.004866	2.81	0.042
P*ET*PD	1	0.006930	0.006930	0.00693	4.00	0.054
P*ET*HS	1	0.00143	0.00143	0.001432	0.83	0.370
P*PD*HS	1	1.9E-05	1.9E-05	1.93E-05	0.01	0.917
ET*PD*HS	1	0.01108	0.01108	0.0110830	6.40	0.017
Residual Error	31	0.05368	0.05368	0.001732		
Total	47	0.35257				

To gain further insight on the effects of machine parameters and their interactions, an Interactions Plot was made and can be seen in Figure 5.37. The significant interaction of power and exposure time shows that at high power increasing exposure time decreases part density and at low power it increases it. Taking note that for the single line scans exposure time has no effect on geometry, but at the high power level it has an effect on density, it can be concluded that this is an indication of keyhole induced porosity at high exposure times. The interaction for power and point distance shows that at high power increasing point distance decreases density, and at low power the opposite occurs. The interaction between power and hatch spacing, while not significant, does begin to explain the opposite results for the previously mentioned interactions. Here it can be seen that at high power increasing the hatch spacing decreases the part density, but at low power hatch spacing has no effect and the recorded value is significantly lower than that for the high power. What this shows is that the hatch spacing was too large for the low power even though the experiment was designed to only have point distance of 25% of the spot size. Taking into account the melt pool size at 100W, should have been sufficient to still have overlap between hatches. This shows the sensitivity of increasing hatch spacing beyond the distance of the laser spot size.

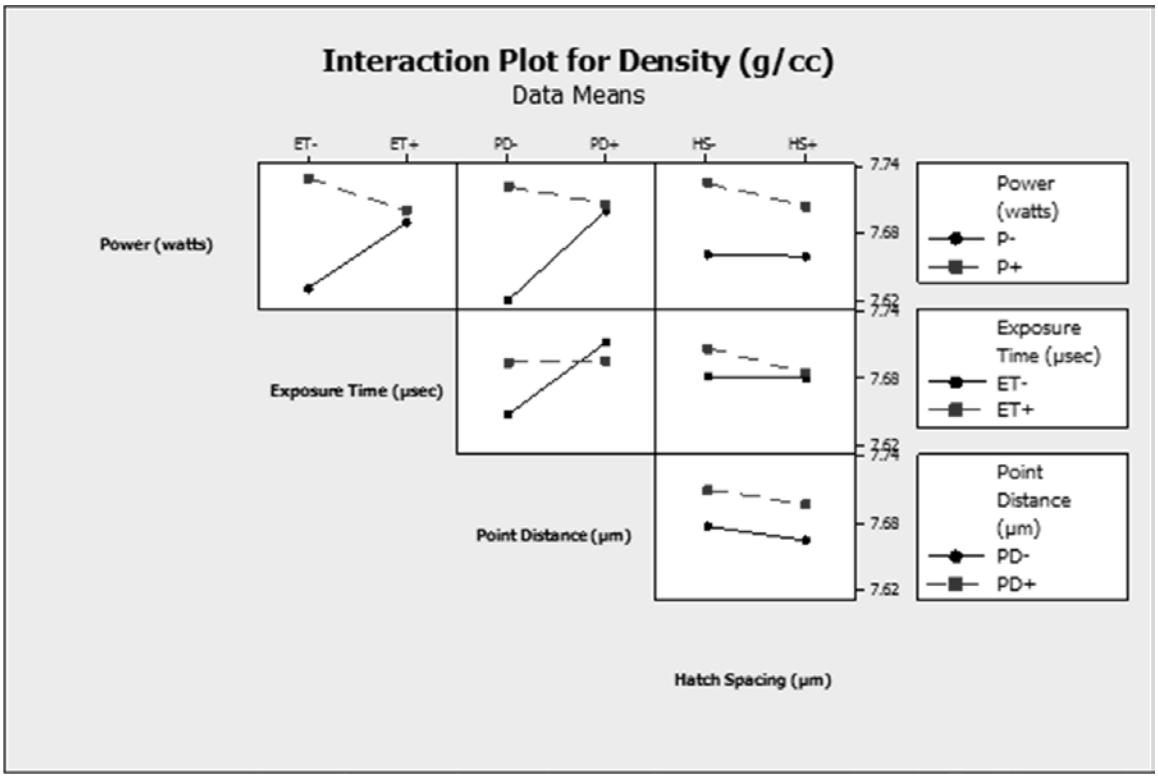

Figure 5.37: 2 Level DOE Interaction Plot for Density

The data collect from the three lots is combined and can be found in Figure 5.38. Although this data exhibits a fairly high variance, the same general trend of increasing energy input resulting in an increasing part density to a point as discussed in Section 1.2.3. The high variance can be attributed to the build orientation of the density cubes. Although a 45° orientation allowed for easy removal from the plate and eliminated the effect of a machined surface, the down facing surfaces created variance due to the laser over melting into loose powder and collecting material from the bed.

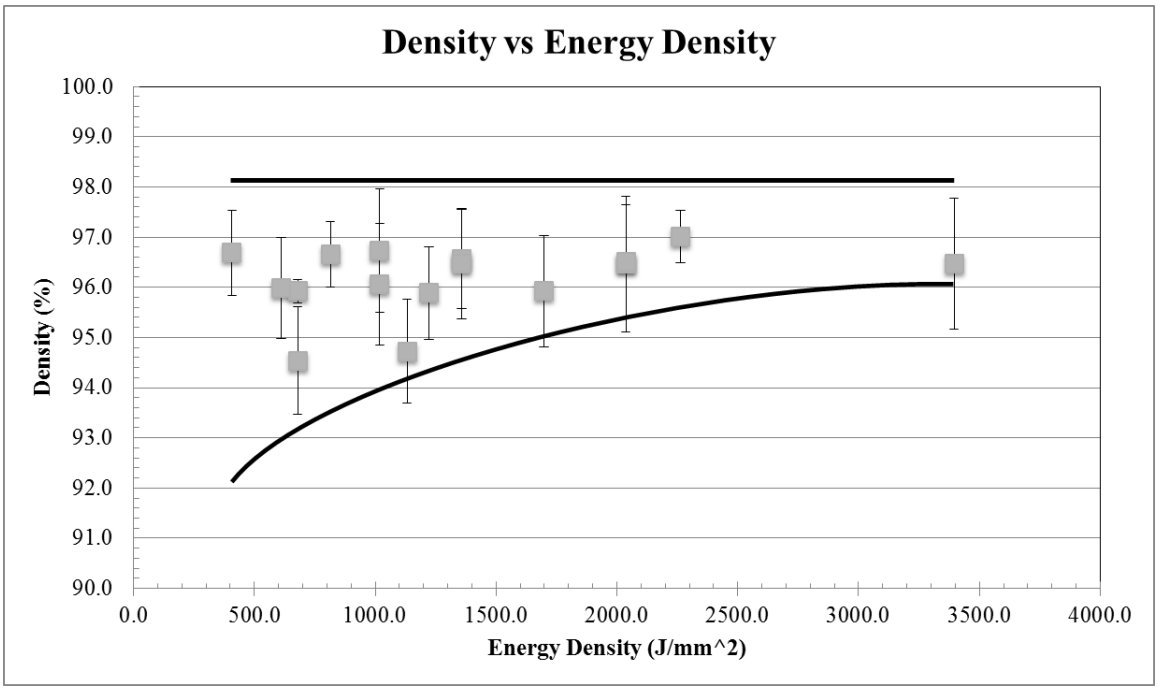

Figure 5.38: 2 Level DOE Data

5.5 OPTIMIZED PARAMETERS

Based on the results of the single line scans and density cubes, parameter sets for tensile bars were developed. Two power levels were evaluated; 200W and 125 W. 200 W was selected as it the highest output power on the machine. 125W was selected as it was the minimum power to achieve 50µm penetration depth. Set 1 uses the optimal machine parameters as determined from the density DOE. Sets 2 and 3 have all the same parameters, except for the decrease of exposure time to out of the tested region, resulting in an increased speed and lower energy density. The parameter of exposure time was selected for reduction as the trend exhibited by the interactions plot showed increasing

hatch spacing and point distance would reduce density at high laser power. From Figure 5.38, the apparent cusp for this material lies at a $E_{\rho 2}$ between 1500 and 2000 $\frac{\mathrm{J}}{\mathrm{mm}^2}$.

Parameters for 125 W beginning with Set 4 was also based off the ideal from the DOE, except the hatch spacing was reduced due to the single line geometry effects at lower power. The point distance used was the large value tested in the DOE as it resulted in the highest density part. The selected hatch spacing for the 200 W parameters is roughly a 30% overlap. Using the determined regression equation for width at the laser power of 125 W, a hatch spacing of 37 um was calculated as a 30% overlap. The same equivalent speeds were used from the 200 W parameters and exposure time was reduced to match. A full summary of the 10 parameter sets used can be found in Tables 5.5 through 5.7. In addition to the 4 machine parameters, each parameter set included the speed that a single line is being scanned at, the energy density, and the time to scan a specific area of 1 mm^2. The 10 sets were built on two separate builds. Parameter set 10 failed and was not able to be completed.

Table 5.5: Tensile Bar Parameter Set Summary

Set 1 (BUILD 6)			**Set 4 (BUILD 6)**	
P (watts)	200.0		**P (watts)**	125.0
HS (µm)	52.5		**HS (µm)**	37.0
ET (µsec)	120.0		**ET (µsec)**	180.0
PD (µm)	52.5		**PD (µm)**	87.5
Speed (mm/s)	437.5		**Speed (mm/s)**	486.1
ED (J/mm^2)	2263.7		**ED (J/mm^2)**	1806.8
Specific Area Time (Sec)	0.0435		**Specific Area Time (Sec)**	0.0556
Set 2 (BUILD 6)			**Set 5 (BUILD 6)**	
P (watts)	200.0		**P (watts)**	125.0
HS (µm)	52.5		**HS (µm)**	37.0
ET (µsec)	82.2		**ET (µsec)**	137.0
PD (µm)	52.5		**PD (µm)**	87.5
Speed (mm/s)	638.7		**Speed (mm/s)**	638.7
ED (J/mm^2)	1550.7		**ED (J/mm^2)**	1375.2
Specific Area Time (Sec)	0.0298		**Specific Area Time (Sec)**	0.0423

Table 5.5: Tensile Bar Parameter Set Summary (cont.)

Set 3 (BUILD 6)			**Set 6 (BUILD 7)**	
P (watts)	200.0		**P (watts)**	125.0
HS (µm)	52.5		**HS (µm)**	37.0
ET (µsec)	62.6		**ET (µsec)**	104.0
PD (µm)	52.5		**PD (µm)**	87.5
Speed (mm/s)	838.7		**Speed (mm/s)**	841.3
ED (J/mm^2)	1180.9		**ED (J/mm^2)**	1043.9
Specific Area Time (Sec)	0.0227		**Specific Area Time (Sec)**	0.0321
Set 7 (BUILD 7)			**Set 8 (BUILD 7)**	
P (watts)	200.0		**P (watts)**	125.0
HS (µm)	52.5		**HS (µm)**	37.0
ET (µsec)	50.0		**ET (µsec)**	83.3
PD (µm)	52.5		**PD (µm)**	87.5
Speed (mm/s)	1050.0		**Speed (mm/s)**	1050.4
ED (J/mm^2)	943.2		**ED (J/mm^2)**	836.1
Specific Area Time (Sec)	0.0181		**Specific Area Time (Sec)**	0.0257

Table 5.5: Tensile Bar Parameter Set Summary (cont.)

Set 9 (BUILD 7)			Set 10 (BUILD 7)	
P (watts)	200.0		**P (watts)**	125.0
HS (µm)	52.5		**HS (µm)**	37.0
ET (µsec)	35.0		**ET (µsec)**	58.3
PD (µm)	52.5		**PD (µm)**	87.5
Speed (mm/s)	1500.0		**Speed (mm/s)**	1500.9
ED (J/mm^2)	660.3		**ED (J/mm^2)**	585.2
Specific Area Time (Sec)	0.0127		**Specific Area Time (Sec)**	0.0180

A comparison of like machine parameters can be found in Table 5.6. Although many parameters were found in literature, these parameters used a similar power level for the like material of like chemistry, 316L. Regardless of the similarity, the difference in powder properties in addition to the chemical difference causes these materials to behave differently and therefore requiring different machine parameters.

Table 5.6: Parameter Set Comparison

Power (Watts)	PD (µm)	ET (µsec)	Speed (mm/s)	HS (µm)	Source	Material
180	65	110	590	110	Renishaw	316L
200	N/A	N/A	1600	70% overlap	Kamath, C., et al. [62]	316L

5.5.1 Density Results. Density cubes built at the 9 successful parameter sets were removed from the plate by wire EDM. These cubes were built at a 0° orientation as opposed to the 45° as previously used because these samples were intended to be micrographed and the goal was to orient the image perpendicular to the build layer. Building the samples at an angle would have made this an arduous task. Because of the machined surface on the part, at lower energy densities, open porosity could be seen. As previously discussed, once the part is no longer water tight, helium pycnometry is no longer accurate. To validate density determined by helium pycnometry, by optical determination was also used. Results derived by optical correlate well with those for the pycnometry method showing the same trend of higher values that was seen in Section 4.4.1 except for two outliers. These erroneous measurements emphasize the fact that optical methods are not as reliable as the methods previously mentioned and to get reliable results several images need to be taken.

Results are displayed below in Figure 5.39. The samples for the parameter sets derived from the DOE are near full dense and begin to reduce as energy density is decreased. This confirms that the optimal parameter set was located at the cusp discussed

in Section 1.2.3. With the different methods plotted against energy density, it can be seen where the use of helium pycnometry breaks down. As discussed in Section 4.4.1, for helium pycnometry to be an effective method the sample must be water tight. As designated by the dashed line at approximately 96% density, the helium pycnometer begins to return false high values. Likewise, error from the optical method can be seen resulting in a false low value. Disregarding these errors, trends can be seen where the optical shows to return a slightly higher density value over helium pycnometry for these samples.

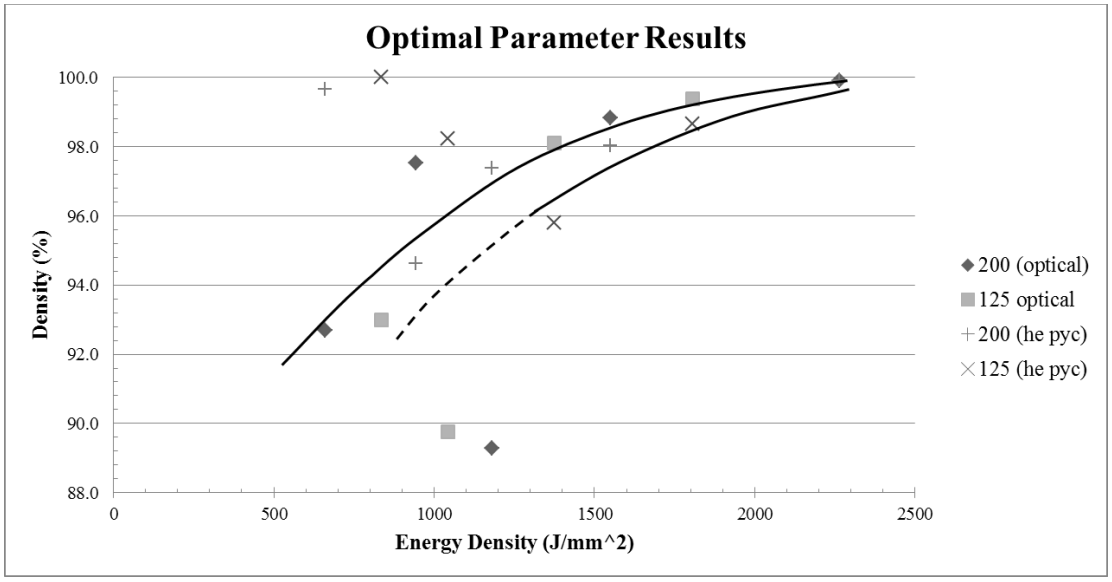

Figure 5.39: Density Results as a Function of Energy Density

When the same data is plotted against exposure time instead of energy density the data begins to separate by laser power. This plot can be seen in Figure 5.40. Per Equation

11, if point distance is constant a decreasing exposure time is an effective increase in scan speed. The data shows that for maximizing build rate, the AM250's build speed is limited by laser power when trying to achieve full density. The results of Kamath et al. [62] on a continuous exposure system show that by increasing laser power, the curve shifts allowing full density to be achieved at faster scan speed. These results show that the same effect can be seen in a spot exposure platform and in order to achieve a faster build rate at full density, a more powerful laser is needed.

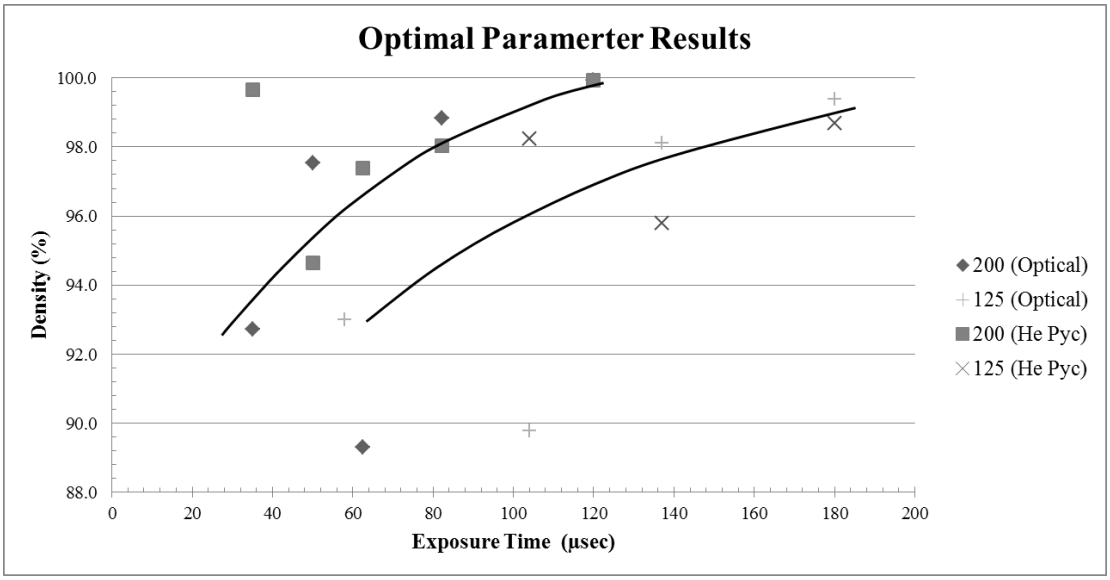

Figure 5.40: Density Results As a Function of Exposure Time

5.5.2 Macro Images. Macro images of samples from sets 1, 4, 8, and 9 can be seen below in Figures 5.41 through 5.48. These represent the highest and lowest energy density parameters sets for the 200 W and 125W parameter sets.

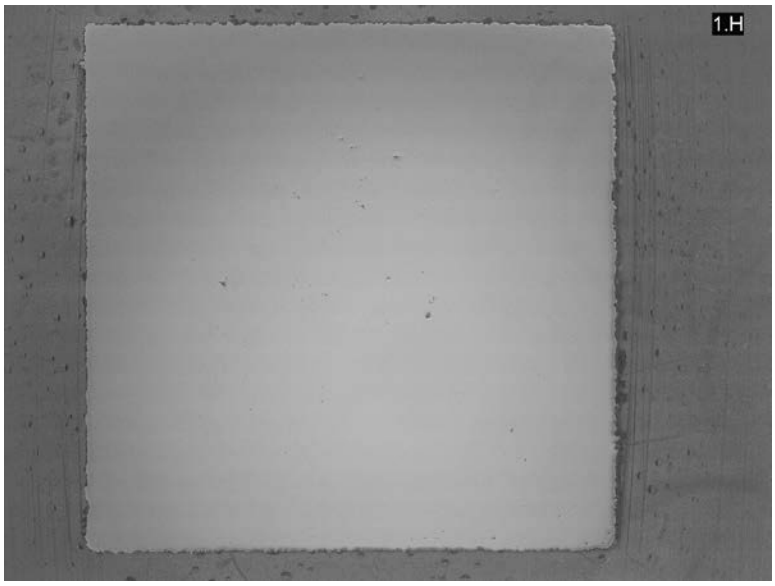

Figure 5.41: Sample 1 Horizontal Cross Section

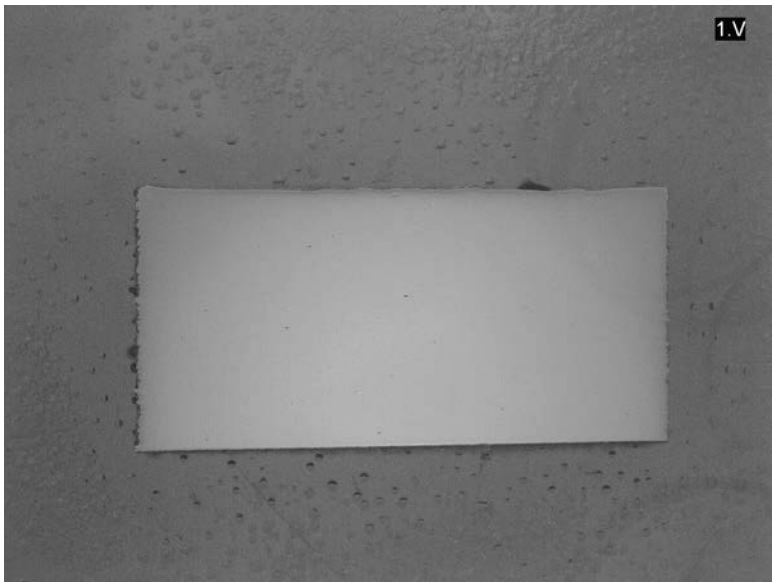

Figure 5.42: Sample 1 Vertical Cross Section

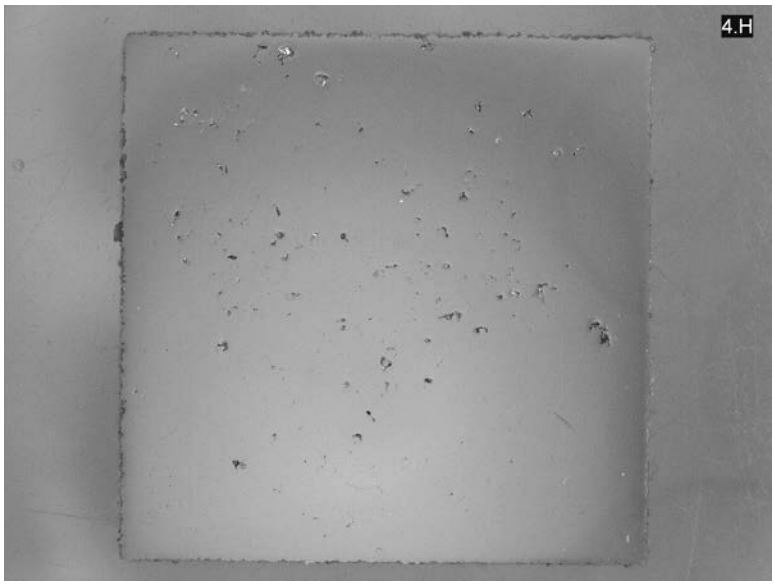

Figure 5.43: Sample 4 Horizontal Cross Section

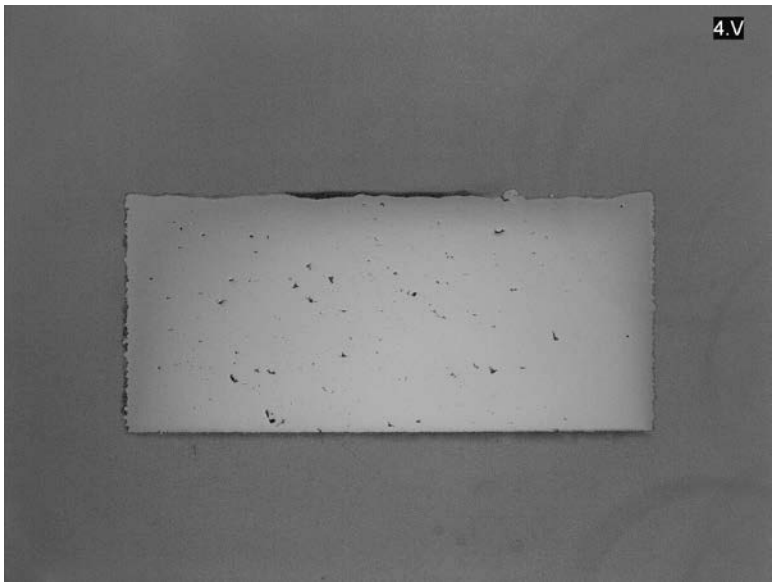

Figure 5.44: Sample 4 Vertical Cross Section

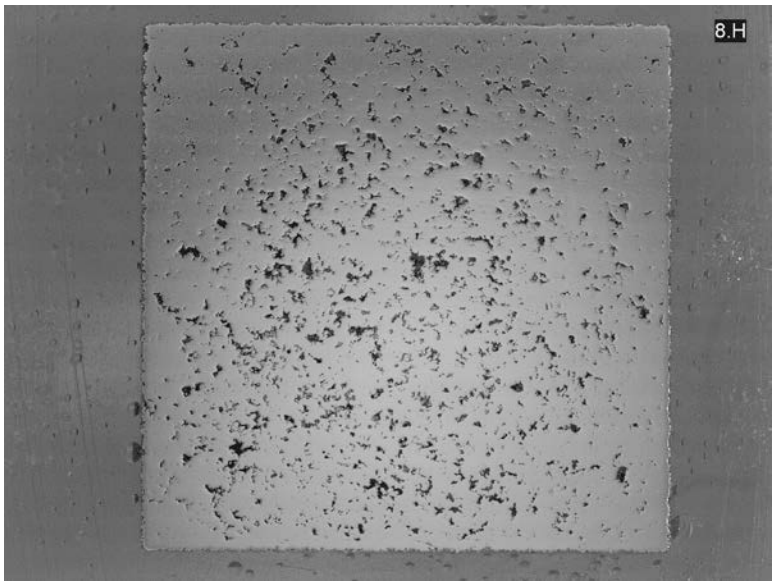

Figure 5.45: Sample 8 Horizontal Cross Section

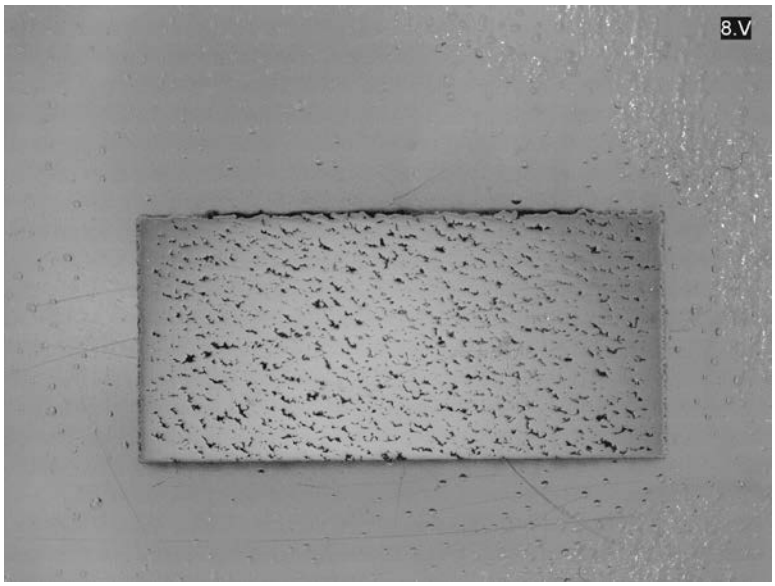

Figure 5.46: Sample 8 Vertical Cross Section

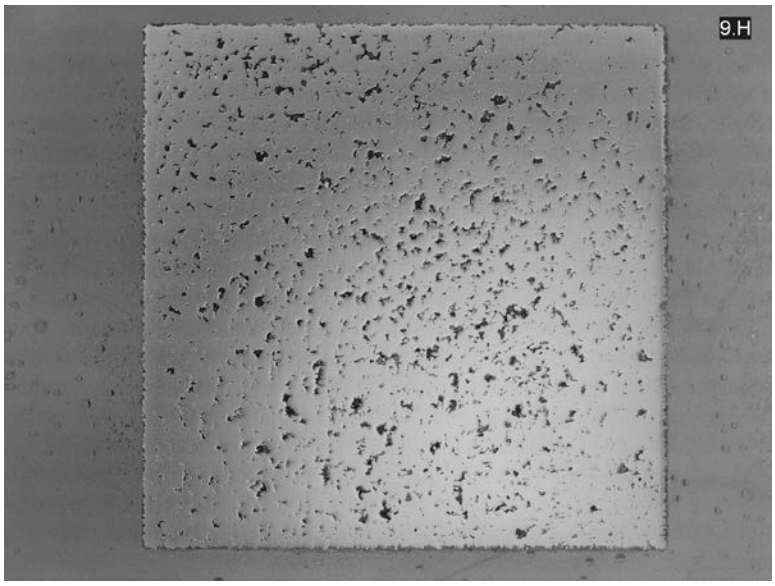

Figure 5.47: Sample 9 Horizontal Cross Section

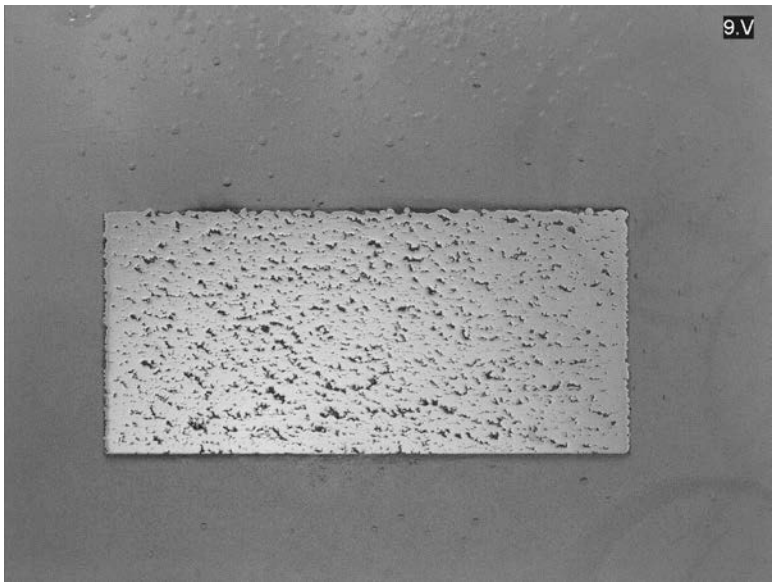

Figure 5.48: Sample 9 Vertical Cross Section

5.5.3 Micrograph Images. Micrograph images of Samples 1, 4, 8, and 9 can be seen below in Figures 5.49 through 5.56. The images from Sample 1 exhibit near full dense with some trace random porosity. For Sample 4 where porosity is more predominate, the porosity in the horizontal view appears to be mostly random, but the porosity in the vertical cross section is constantly at the bottom of the melt pool. This shows that although a regression equation based on single line data was used to determine the power to achieve 50 µm of penetration, the depth is still no enough to get full bonding between layers. For future attempts at low energy parameter sets, a minimum target penetration depth of at least 25% greater than the layer thickness. The images for Samples 8 and 9 clearly show the gross porosity in the parts as the energy input to the part was far too low.

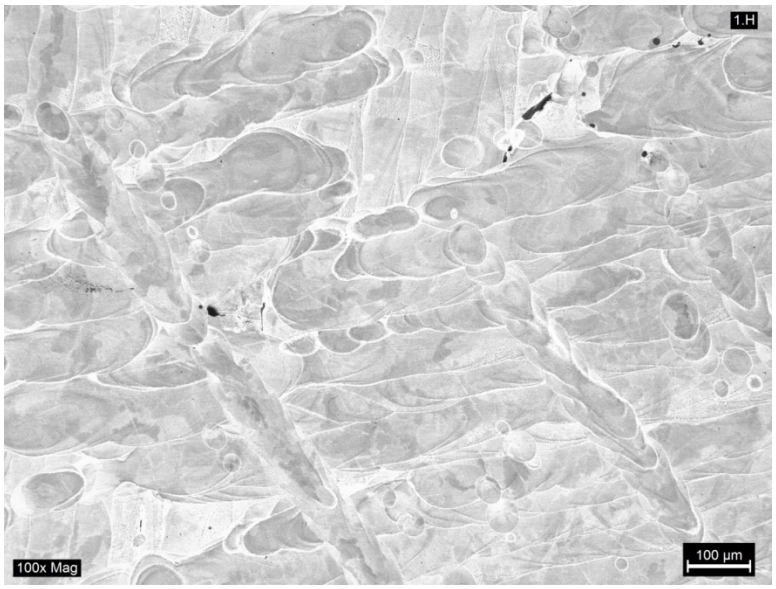

Figure 5.49: Sample 1 Horizontal Cross Section

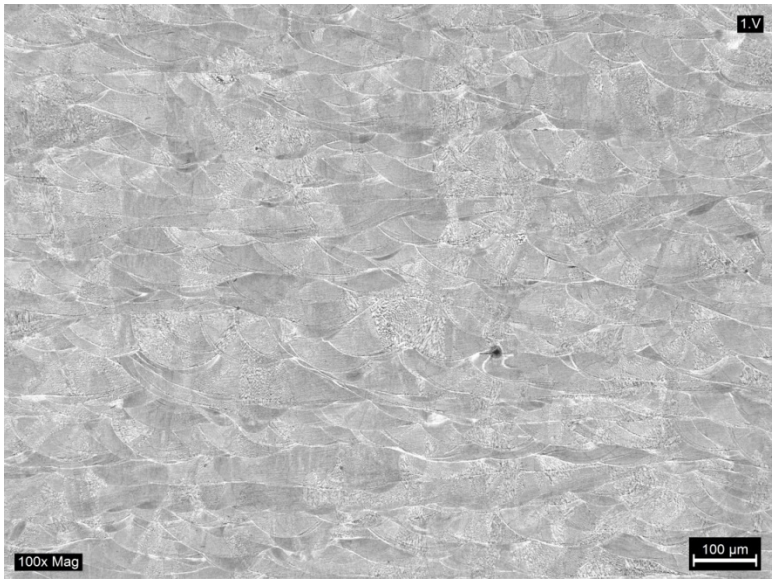

Figure 5.50: Sample 1 Vertical Cross Section

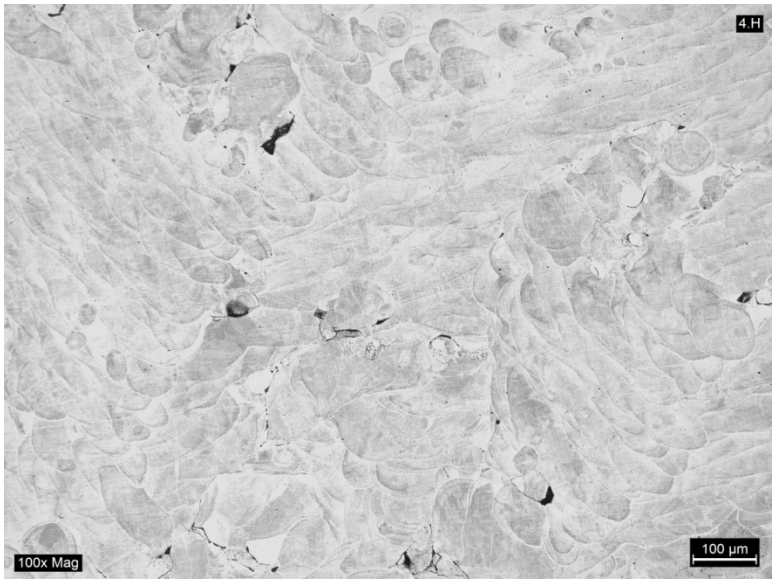

Figure 5.51: Sample 4 Horizontal Cross Section

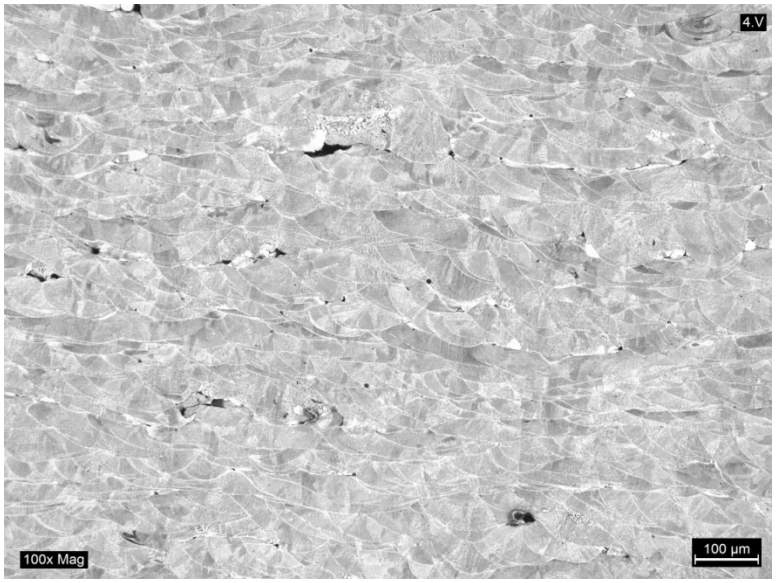

Figure 5.52: Sample 4 Vertical Cross Section

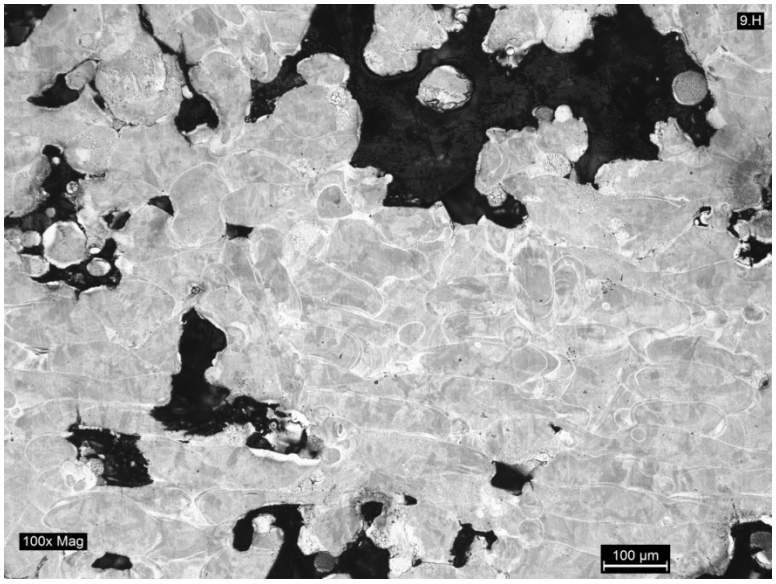

Figure 5.53: Sample 9 Horizontal Cross Section

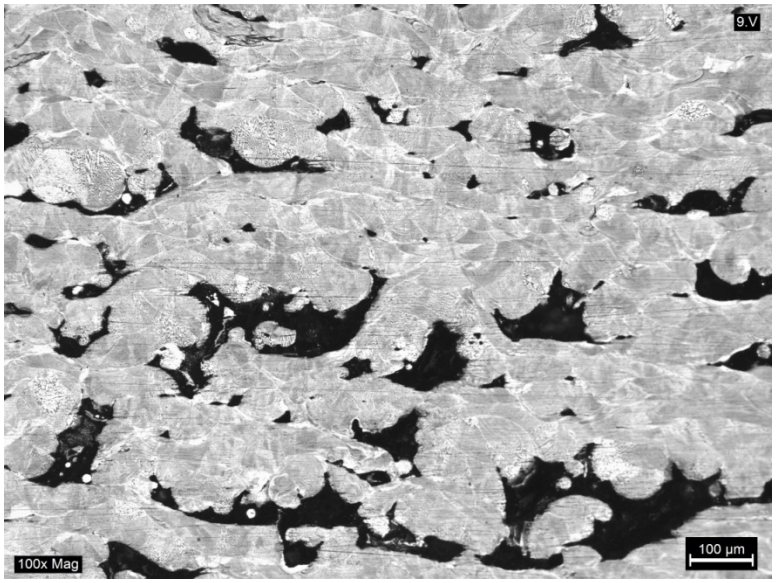

Figure 5.54: Sample 9 Vertical Cross Section

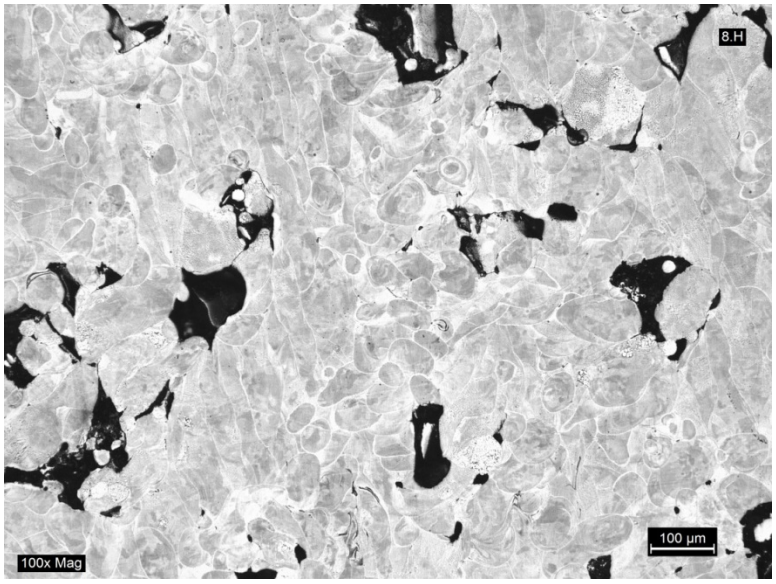

Figure 5.55: Sample 8 Horizontal Cross Section

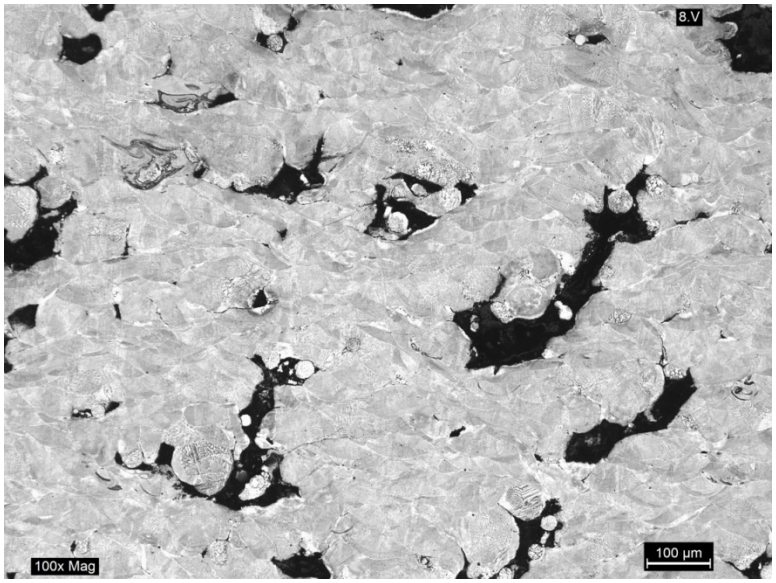

Figure 5.56: Sample 8 Vertical Cross Section

5.5.4 Tensile Results. The results for the parameter sets can be seen below in Figure 5.57 for the 200W sets and Figure 5.58 for the 125W sets. Build orientation is displayed and standard deviation is shown by error bars. Elongation at break for each orientation at each parameter set is also found above each set of bars.

It can be seen that for all parameter sets that as the energy density for the corresponding parameter set is decreased the Ultimate Tensile Strength (UTS) decreases as well. This is directly related to the increasing porosity that was discussed in the previous sections. Over the range tested, there is consistent decline in UTS and no change in the anisotropic behavior. Higher tensile strength in the horizontal build direction as seen here is a common occurrence in all the literature surveyed. However, the 125W parameters do show more directional sensitivity than the 200 W parameters. This reduction in vertical build orientation tensile strength for the 125 W parameters can be attributed to the low penetration depth, as discussed in Section 5.5.3. Variance for the 200 W parameters are low compared to the 125 W parameters.

For the 200 W parameters, Sets 1, 2, 3, and 7 in both the vertical and horizontal built orientations are close to or above the standard minimum UTS for 304L of 70 ksi. Elongation at break values show the same trend as UTS where the values for the horizontally built samples tend to be slightly higher than the vertical sample values. Only Set 1 meets the minimum 40% elongation at break per the ASTM standard where all other values fall closer to 20%. In an attempt to increase this value it is parts built could receive a process anneal.

After machining, horizontal samples exhibited some deformation caused by internal stress. When being tested, a nonlinear elastic region on the stress strain curve was recorded as a result. Again, the usage of a heat treatment could be used to minimize this issue.

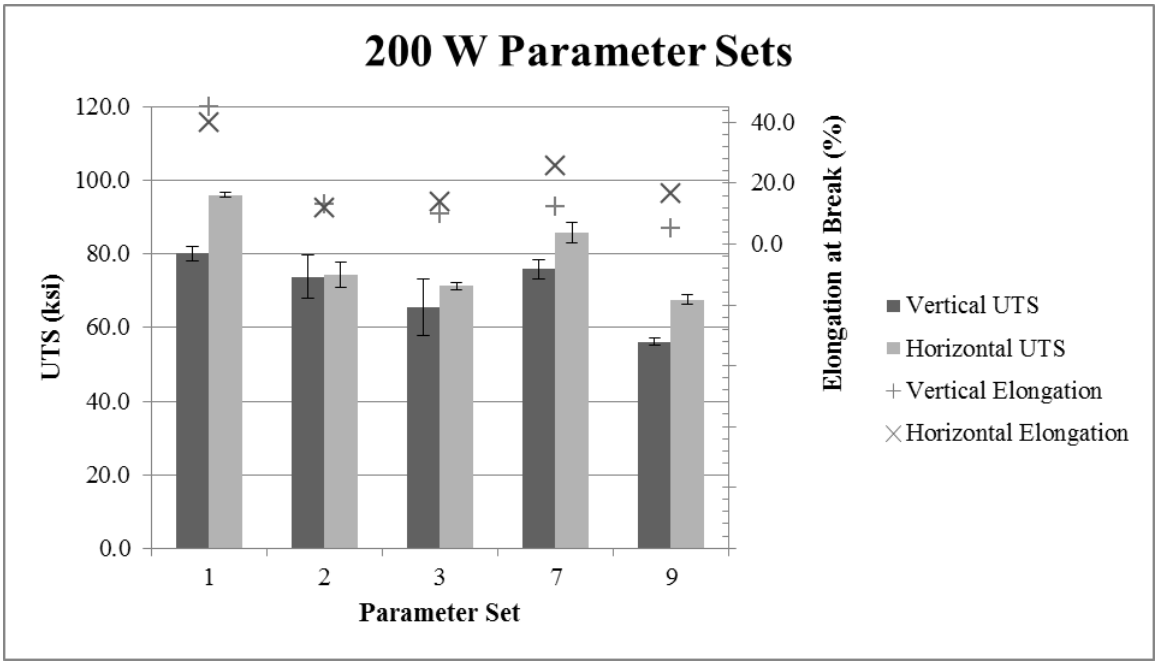

Figure 5.57: 200W Parameter Set Results

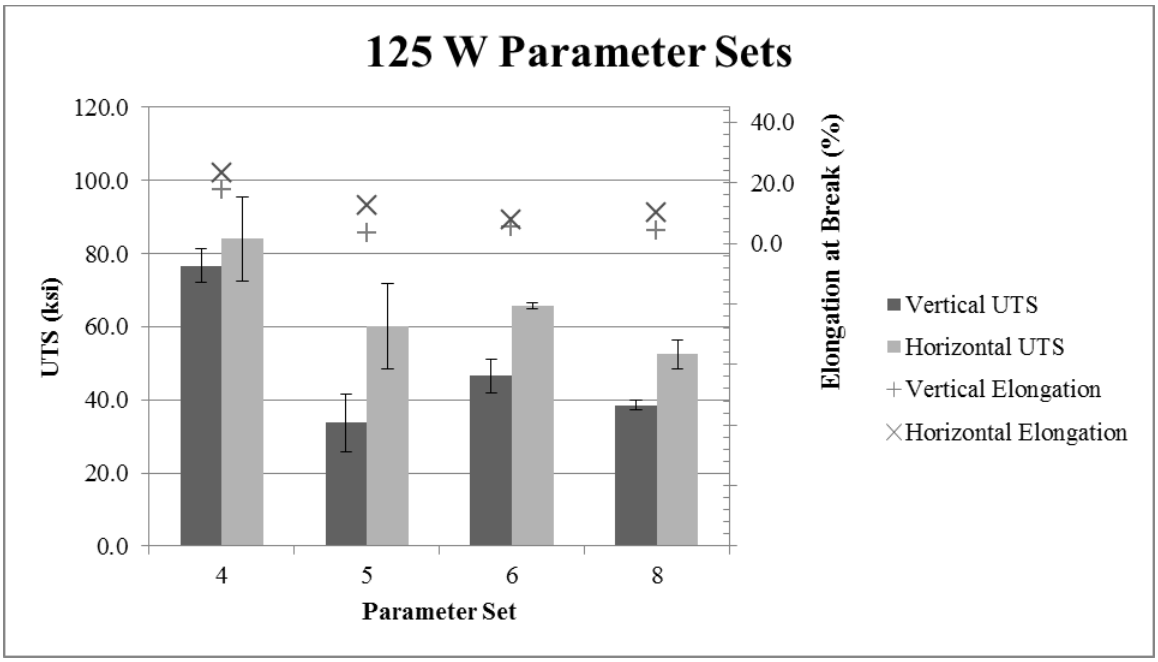

Figure 5.58: 125W Parameter Set Results

Because of the high porosity and less than desirable mechanical properties exhibited by the 125 W Parameter Sets, it is not feasible to use Sets 4, 5, 6, or 8 to produce parts. However, the 200 W Sets would be applicable for part production. Although below full density, Sets 2, 3, and 7 show UTS values at or above the requirement per ASTM and with the addition of a heat treatment the elongation values could be brought into spec. With proper consideration and design these faster parameter sets could be used, even with the determined properties.

6 CONCLUSIONS

In this study parameter sets for a material novel to SLM, 304L stainless steel, were developed. To begin development material was purchased from a specification derived from literature where requirements for size distribution, morphology, and chemistry were defined. The standard characterization procedure was then used where single line scans were used to define the processing window and determine geometric constraints for scan strategy. A DOE was then implemented to determine the main effect factors for achieving full density. Using main effect factors and their interactions, a parameter set that achieved 99+% density was developed. Again, utilizing the determined main effect factors, parameter sets were developed at less than optimized parameter to determine at what minimum energy density test samples no longer meet the requirements of ASTM A240. It was shown that the optimal parameter set met the requirements for ASTM A240 for type 304L. For the remaining parameter sets, UTS met the standard requirements for most sets but the elongation a break value was below minimum value per the ASTM spec. In order to meet the elongation requirement, a post process heat treatment is required. It was shown that over the range tested that with the reduction of energy density from the determined optimal amount, part porosity increased and mechanical properties decreased. By testing the reduced energy parameter sets, sensitivity to density reduction for mechanical properties was shown to be minimal. It was also shown that reducing energy density does not reduce anisotropic mechanical behavior.

Overall, it was shown that by using a statistical method for determining optimal machine parameters, full dense part can be achieved on a spot exposure SLM platform

and that by using an energy input less that optimal close to desirable mechanical properties can be achieved.

APPENDIX
Tooling Drawings

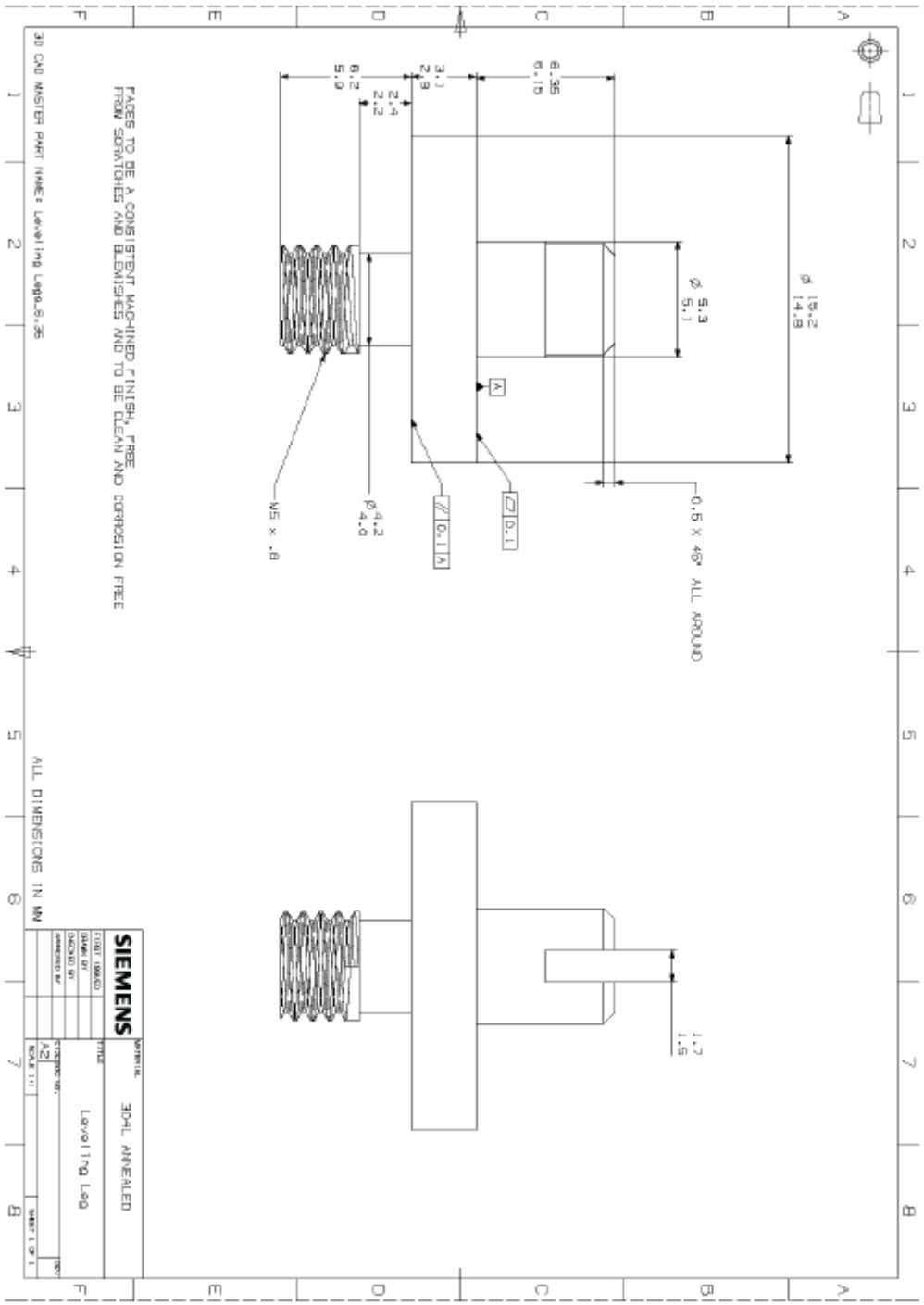

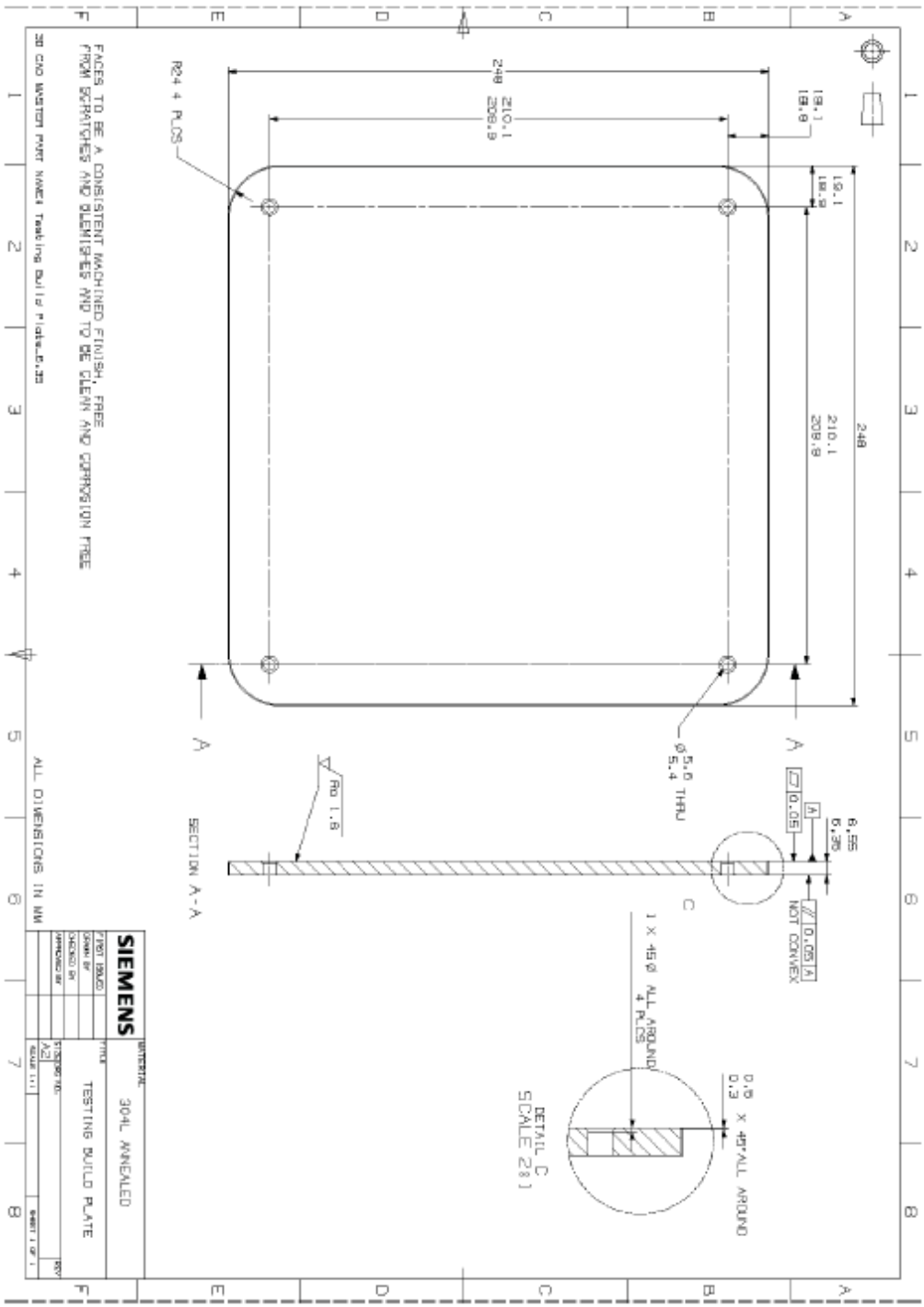

REFERENCES

1. Wohlers, T. and T. Gornet, *History of Additive Manufacturing*. 2013.

2. Wehmöller, M., et al., *Implant design and production—a new approach by selective laser melting.* International Congress Series, 2005. **1281**(0): p. 690-695.

3. Takaichi, A., et al., *Microstructures and mechanical properties of Co–29Cr–6Mo alloy fabricated by selective laser melting process for dental applications.* Journal of the Mechanical Behavior of Biomedical Materials, 2013. **21**(0): p. 67-76.

4. Wu, L., et al., *Evaluation of the mechanical properties and porcelain bond strength of cobalt-chromium dental alloy fabricated by selective laser melting.* The Journal of Prosthetic Dentistry, 2014. **111**(1): p. 51-55.

5. Associates, W.a., *Wohlers Report*. 2013.

6. Guo, N. and M.C. Leu, *Additive manufacturing: technology, applications and research needs.* Frontiers of Mechanical Engineering, 2013. **8**(3): p. 215-243.

7. Santos, E.C., et al., *Rapid manufacturing of metal components by laser forming.* International Journal of Machine Tools and Manufacture, 2006. **46**(12-13): p. 1459-1468.

8. Simchi, A., F. Petzoldt, and H. Pohl, *On the development of direct metal laser sintering for rapid tooling.* Journal of Materials Processing Technology, 2003. **141**(3): p. 319-328.

9. Frazier, W.E., *Metal Additive Manufacturing: A Review*. Journal of Materials Engineering and Performance, 2014. **23**(6): p. 1917-1928.

10. Averyanova, M., et al., *Experimental design approach to optimize selective laser melting of martensitic 17-4 PH powder: part I – single laser tracks and first layer.* Rapid Prototyping Journal, 2012. **18**(1): p. 28-37.

11. Zhang, B., H. Liao, and C. Coddet, *Effects of processing parameters on properties of selective laser melting Mg–9%Al powder mixture.* Materials & Design, 2012. **34**: p. 753-758.

12. Sun, J., Y. Yang, and D. Wang, *Parametric optimization of selective laser melting for forming Ti6Al4V samples by Taguchi method.* Optics & Laser Technology, 2013. **49**: p. 118-124.

13. Kruth, J.P., S. Kumar, and J.V. Vaerenbergh, *Study of laser-sinterability of ferro-based powders.* Rapid Prototyping Journal, 2005. **11**(5): p. 287-292.

14. Simchi, A. and H. Pohl, *Effects of laser sintering processing parameters on the microstructure and densification of iron powder.* Materials Science and Engineering: A, 2003. **359**(1-2): p. 119-128.

15. Simchi, A., *Direct laser sintering of metal powders: Mechanism, kinetics and microstructural features.* Materials Science and Engineering: A, 2006. **428**(1-2): p. 148-158.

16. Yadroitsev, I., P. Bertrand, and I. Smurov, *Parametric analysis of the selective laser melting process.* Applied Surface Science, 2007. **253**(19): p. 8064-8069.

17. Mumtaz, K.A., P. Erasenthiran, and N. Hopkinson, *High density selective laser melting of Waspaloy®.* Journal of Materials Processing Technology, 2008. **195**(1-3): p. 77-87.

18. Gu, D. and Y. Shen, *Balling phenomena in direct laser sintering of stainless steel powder: Metallurgical mechanisms and control methods.* Materials & Design, 2009. **30**(8): p. 2903-2910.

19. Gu, D. and Y. Shen, *Effects of processing parameters on consolidation and microstructure of W–Cu components by DMLS.* Journal of Alloys and Compounds, 2009. **473**(1-2): p. 107-115.

20. Yadroitsev, I., et al., *Single track formation in selective laser melting of metal powders.* Journal of Materials Processing Technology, 2010. **210**(12): p. 1624-1631.

21. Yang, Y., *Accuracy and density optimization in directly fabricating customized orthodontic production by selective laser melting.* Rapid Prototyping Journal, 2012. **18**(6): p. 482-489.

22. Monroy, K., J. Delgado, and J. Ciurana, *Study of the Pore Formation on CoCrMo Alloys by Selective Laser Melting Manufacturing Process.* Procedia Engineering, 2013. **63**(0): p. 361-369.

23. Pupo, Y., et al., *Scanning Space Analysis in Selective Laser Melting for CoCrMo Powder.* Procedia Engineering, 2013. **63**(0): p. 370-378.

24. Zhang, L.C., et al., *Manufacture by selective laser melting and mechanical behavior of a biomedical Ti–24Nb–4Zr–8Sn alloy.* Scripta Materialia, 2011. **65**(1): p. 21-24.

25. Yadroitsev, I., et al., *Energy input effect on morphology and microstructure of selective laser melting single track from metallic powder.* Journal of Materials Processing Technology, 2013. **213**(4): p. 606-613.

26. Thijs, L., et al., *A study of the microstructural evolution during selective laser melting of Ti–6Al–4V.* Acta Materialia, 2010. **58**(9): p. 3303-3312.

27. Song, B., et al., *Microstructure and tensile properties of iron parts fabricated by selective laser melting.* Optics & Laser Technology, 2014. **56**: p. 451-460.

28. Olakanmi, E.O., *Selective laser sintering/melting (SLS/SLM) of pure Al, Al–Mg, and Al–Si powders: Effect of processing conditions and powder properties.* Journal of Materials Processing Technology, 2013. **213**(8): p. 1387-1405.

29. Mercelis, P. and J.-P. Kruth, *Residual stresses in selective laser sintering and selective laser melting.* Rapid Prototyping Journal, 2006. **12**(5): p. 254-265.

30. Kruth, J.P., et al., *Selective laser melting of iron-based powder.* Journal of Materials Processing Technology, 2004. **149**(1-3): p. 616-622.

31. Yasa, E. and J.P. Kruth, *Microstructural investigation of Selective Laser Melting 316L stainless steel parts exposed to laser re-melting.* Procedia Engineering, 2011. **19**: p. 389-395.

32. Kempen, K., et al., *Microstructure and mechanical properties of Selective Laser Melted 18Ni-300 steel.* Physics Procedia, 2011. **12**: p. 255-263.

33. Kempen, K., et al. *Process Optimization and Microstructural Analysis for Selective Laser Melting of AlSi10Mg*. in *Proceedings of the Annual International Solid Freeform Fabrication Symposium*. 2011.

34. Das, S., et al., *Producing metal parts with selective laser sintering/hot isostatic pressing.* JOM, 1998. **50**(12): p. 17-20.

35. Simchi, A., *The Role of Particle Size on the Laser Sintering of Iron Powder.* Metallurgical and Materials Transactions B, 2004. **35B**: p. 937-948.

36. Gu, D. and Y. Shen, *Balling phenomena during direct laser sintering of multi-component Cu-based metal powder.* Journal of Alloys and Compounds, 2007. **432**(1-2): p. 163-166.

37. Morgan, R., C.J. Sutcliffe, and W. O'Neill, *Density Analysis of Direct Metal Laser Re-Melted 316L Stainless Steel Cubic Primitves* Journal of Materials Science, 2004. **39**: p. 1195-1205.

38. Spierings, A. and G. Levy. *Comparison of density of stainless steel 316L parts produced with selective laser melting using different powder grades*. in *Proceedings of the Annual International Solid Freeform Fabrication Symposium*. 2009.

39. Starr, T.L., et al. *Controlling Phase Composition in Selective Laser Melted Stainless Steels*. in *Proceedings of the Annual International Solid Freeform Fabrication Symposium*. 2012.

40. Childs, T.H.C., C. Hauser, and M. Badrossamay, *Mapping and Modelling Single Scan Track Formation in Direct Metal Selective Laser Melting.* CIRP Annals - Manufacturing Technology, 2004. **53**(1): p. 191-194.

41. Badrossamay, M. and T.H.C. Childs, *Further studies in selective laser melting of stainless and tool steel powders.* International Journal of Machine Tools and Manufacture, 2007. **47**(5): p. 779-784.

42. Gu, H., et al. *Influences of Energy Density on Porosity and Microstructure of Selective Laser Melted 17-4PH Stainless Steel*. in *Proceedings of the Annual International Solid Freeform Fabrication Symposium*. 2013.

43. Ng, C.C., M. Savalani, and H.C. Man, *Fabrication of magnesium using selective laser melting technique.* Rapid Prototyping Journal, 2011. **17**(6): p. 479-490.

44. Gong, H., et al. *Effect of Defects on Fatigue Tests of As-Built Ti-6Al-4V Parts Fabricated by Selective Lasser Melting*. in *Proceedings of the Annual International Solid Freeform Fabrication Symposium*. 2012.

45. King, W.E., et al., *Observation of keyhole-mode laser melting in laser powder-bed fusion additive manufacturing.* Journal of Materials Processing Technology, 2014.

46. He, X., P.W. Fuerschbach, and T. DebRoy, *Heat transfer and fluid flow during laser spot welding of 304 stainless steel.* Journal of Physics D: Applied Physics, 2003. **36**(12): p. 1388.

47. Assuncao, E. and S. Williams, *Comparison of continuous wave and pulsed wave laser welding effects.* Optics and Lasers in Engineering, 2013. **51**(6): p. 674-680.

48. De, A. and T. DebRoy, *Improving reliability of heat and fluid flow calculation during conduction mode laser spot welding by multivariable optimisation.* Science and Technology of Welding and Joining, 2006. **11**(2): p. 143-153.

49. Ho, H.C.H., I. Gibson, and W.L. Cheung, *Effects of Energy Density on Morphology and Properties of Selective Laser Sintered Polycarbonate.* Journal of Materials Processing Technology, 1999. **89-90**: p. 204-210.

50. Ng, C.C., et al., *Microstructure and mechanical properties of selective laser melted magnesium.* Applied Surface Science, 2011. **257**(17): p. 7447-7454.

51. Niendorf, T., et al., *Functionally Graded Alloys Obtained by Additive Manufacturing.* Advanced Engineering Materials, 2014.

52. Carter, L.N., et al., *The Influence of the Laser Scan Strategy on Grain Structure and Cracking Behaviour in SLM Powder-Bed Fabricated Nickel Superalloy.* Journal of Alloys and Compounds, 2014.

53. Starr, T.L., T.J. Gornet, and J.S. Usher, *The effect of process conditions on mechanical properties of laser-sintered nylon.* Rapid Prototyping Journal, 2011. **17**(6): p. 418-423.

54. Zok, F., F.F. Lange, and J.R. Porter, *Packing Density of Composite Powder Mixtures.* Journal of the American Ceramic Society, 1991. **74**(8): p. 1880-1885.

55. Spierings, A., N. Herres, and G. Levy, *Influence of the particle size distribution on surface quality and mechanical properties in AM steel parts.* Rapid Prototyping Journal, 2011. **17**(3): p. 195-202.

56. Karapatis, N., et al. *Optimization of powder layer density in selective laser sintering*. in *Proc. of the 9th Solid Freeform Fabrication Symposium*. 1999.

57. Grey, R.O. and J.K. Beddow, *On the Hausner Ratio and its Relationship to Some Properties of Metal Powders.* Powder Technology, 1969. **2**: p. 323-326.

58. Rombouts, M., et al., *Fundamentals of Selective Laser Melting of alloyed steel powders.* CIRP Annals - Manufacturing Technology, 2006. **55**(1): p. 187-192.

59. Averyanova, M., P. Bertrand, and B. Verquin, *Studying the influence of initial powder characteristics on the properties of final parts manufactured by the selective laser melting technology.* Virtual and Physical Prototyping, 2011. **6**(4): p. 215-223.

60. Spierings, A.B., M. Schneider, and R. Eggenberger, *Comparison of density measurement techniques for additive manufactured metallic parts.* Rapid Prototyping Journal, 2011. **17**(5): p. 380-386.

61. Guan, K., et al., *Effects of processing parameters on tensile properties of selective laser melted 304 stainless steel.* Materials & Design, 2013. **50**(0): p. 581-586.

62. Kamath, C., et al., *Density of additively-manufactured, 316L SS parts using laser powder-bed fusion at powers up to 400 W.* The International Journal of Advanced Manufacturing Technology, 2014. **74**(1-4): p. 65-78.

VITA

Ben Brown was born in Kansas City, Missouri August 1st, 1989. He graduated from Lee's Summit High School in 2008. From high school, Ben pursued a Bachelor of Science degree in Mechanical Engineering at Missouri University of Science and Technology and graduated Cum Laude in December of 2012. At Missouri S&T Ben was a member of Pi Tau Sigma honor society and became a member of The Order of the Engineer. After graduation, Ben began working at Honeywell in Kansas City and after less than a year began a Master's degree program in Manufacturing Engineering at Missouri University of Science and Technology in the fall of 2013. Ben completed his Master's program in December of 2014, under the guidance and direction of Dr. Frank Liou, Dr. Joseph Newkirk, and Dr. Edward Kinzel.